

PLANETARY SCIENCE

Microstructural and chemical features of impact melts on Ryugu particle surfaces: Records of interplanetary dust hit on asteroid Ryugu

Megumi Matsumoto^{1*}, Junya Matsuno², Akira Tsuchiyama^{2,3,4}, Tomoki Nakamura¹, Yuma Enokido¹, Mizuha Kikuri¹, Aiko Nakato⁵, Masahiro Yasutake⁶, Kentaro Uesugi⁶, Akihisa Takeuchi⁶, Satomi Enju⁷, Shota Okumura⁸, Itaru Mitsukawa⁸, Mingqi Sun^{3,4}, Akira Miyake⁸, Mitsutaka Haruta⁹, Yohei Igami⁸, Hisayoshi Yurimoto¹⁰, Takaaki Noguchi⁸, Ryuji Okazaki¹¹, Hikaru Yabuta¹², Hiroshi Naraoka¹¹, Kanako Sakamoto⁵, Shogo Tachibana¹³, Michael Zolensky¹⁴, Toru Yada⁵, Masahiro Nishimura⁵, Akiko Miyazaki⁵, Kasumi Yogata⁵, Masanao Abe⁵, Tatsuaki Okada⁵, Tomohiro Usui⁵, Makoto Yoshikawa⁵, Takanao Saiki⁵, Satoshi Tanaka⁵, Fuyuto Terui¹⁵, Satoru Nakazawa⁵, Sei-ichiro Watanabe¹⁶, Yuichi Tsuda⁵

The Hayabusa2 spacecraft delivered samples of the carbonaceous asteroid Ryugu to Earth. Some of the sample particles show evidence of micrometeoroid impacts, which occurred on the asteroid surface. Among those, particles A0067 and A0094 have flat surfaces on which a large number of microcraters and impact melt splashes are observed. Two impact melt splashes and one microcrater were analyzed to unveil the nature of the objects that impacted the asteroid surface. The melt splashes consist mainly of Mg-Fe-rich glassy silicates and Fe-Ni sulfides. The microcrater trapped an impact melt consisting mainly of Mg-Fe-rich glassy silicate, Fe-Ni sulfides, and minor silica-rich glass. These impact melts show a single compositional trend indicating mixing of Ryugu surface materials and impactors having chondritic chemical compositions. The relict impactor in one of the melt splashes shows mineralogical similarity with anhydrous chondritic interplanetary dust particles having a probable cometary origin. The chondritic micrometeoroids probably impacted the Ryugu surface during its residence in a near-Earth orbit.

INTRODUCTION

Solar System small bodies are believed to be remnants of planet formation and preserve primitive planetary materials. As small bodies lack protective atmospheres, their surface layers are directly exposed to space and suffer modifications collectively called space weathering. Micrometeoroid bombardment and solar wind irradiation are major causes of space weathering, changing chemical compositions, microstructures, and optical properties of regolith particles (1–9). Previous studies of lunar and asteroid Itokawa samples and regolith breccia meteorites revealed various space weathering features including amorphization of crystalline grain surfaces and microcraters and

amorphous deposits on regolith surfaces (1–7, 10). High-velocity micrometeoroid impacts form microcraters and induce vaporization and melting of regolith particles (4, 5, 10, 11). The vaporized and the melted materials form amorphous deposits on the regolith surfaces. These amorphous deposits are expected to have been sourced from both small bodies and micrometeoroid impactors, and detailed characterization of these would allow us to reveal natures of impactors. However, because of the limited amounts of occurrence of amorphous deposits in available planetary samples, natures and origins of micrometeoroids impacting small bodies have been poorly constrained.

The carbonaceous asteroid (162173) Ryugu is a rubble pile composed of reaccumulated fragments of a large parent asteroid formed and disaggregated in the early Solar System (12–14). Large boulders and finer regolith particles covering the asteroid surface show nearly uniform reflectance spectra suggesting minimal compositional diversity, except for some bright boulders (13–15). The Hayabusa2 spacecraft collected surface and subsurface particles (up to ~10 mm in major axis size) from two touchdown sites and delivered these to Earth (16, 17). The particles from the first and the second touchdown sites were separately stored in chambers A and C, respectively (16, 17). The latter possibly contains particles excavated from a depth of ~1 m below the asteroid surface by an artificial impact operation (16, 17). Initial analyses of the returned samples revealed that the particles from the two sites have common chemical and petrological characteristics and consist mainly of magnesium (Mg)-rich phyllosilicates, iron (Fe)-nickel (Ni)-sulfides, magnetite, carbonates, and other minor minerals, which are most similar to Ivuna-type carbonaceous chondrites (CI chondrites) among known meteorite groups (18–22). In the present study, we investigated two Ryugu

¹Department of Earth and Planetary Materials Sciences, Tohoku University, Miyagi 980-8578, Japan. ²Research Organization of Science and Technology, Ritsumeikan University, Shiga 525-8577, Japan. ³Chinese Academy of Sciences (CAS) Key Laboratory of Mineralogy and Metallogeny/Guangdong Provincial Key Laboratory of Mineral Physics and Materials, Guangzhou Institute of Geochemistry, CAS, Guangzhou 510640, China. ⁴CAS Center for Excellence in Deep Earth Science, Guangzhou 510640, China. ⁵Institute of Space and Astronautical Science (ISAS), Japan Aerospace Exploration Agency (JAXA), Sagamihara 252-5210, Japan. ⁶Research and Utilization Division, Japan Synchrotron Radiation Research Institute (JASRI/SPring-8), Hyogo 679-5198, Japan. ⁷Earth's Evolution and Environment Course, Department of Mathematics, Physics, and Earth Science, Ehime University, Ehime 790-8577, Japan. ⁸Division of Earth and Planetary Sciences, Kyoto University, Kyoto 606-8502, Japan. ⁹Institute for Chemical Research, Kyoto University, Gokasho, Uji, Kyoto 611-0011, Japan. ¹⁰Department of Natural History Sciences, Hokkaido University, Sapporo 060-0810, Japan. ¹¹Department of Earth and Planetary Sciences, Kyushu University, Fukuoka 819-0395, Japan. ¹²Graduate School of Advanced Science and Engineering, Hiroshima University, Higashi-Hiroshima 739-8526, Japan. ¹³Department of Earth and Planetary Science, The University of Tokyo, Tokyo 113-0033, Japan. ¹⁴NASA Johnson Space Center, Houston, TX 77058, USA. ¹⁵Department of Mechanical Engineering, Kanagawa Institute of Technology, Atsugi 243-0292, Japan. ¹⁶Department of Earth and Environmental Sciences, Nagoya University, Nagoya 464-8601, Japan. *Corresponding author. Email: m_matsumoto@tohoku.ac.jp

particles, A0067 and A0094, which were collected from the surface of first touchdown site. Each particle has been reported to show evidence of exposure to space and has flat surfaces, which exhibit microcraters and impact melt splashes (19, 20). Relatively large microcraters and melt splashes were selected for microstructural and chemical analyses by field emission scanning electron microscopy (FE-SEM), x-ray nanotomography (XnCT), scanning transmission electron microscopy (STEM), energy-dispersive x-ray spectroscopy (EDS), and electron energy-loss spectroscopy (EELS). Here, we discuss the formation of the microcraters and impact melts and the nature of the impactors that made them. The results showed that the objects formed by impacts of chondritic micrometeoroids.

RESULTS

Flat surfaces of Ryugu A0067 and A0094 particles

The areal sizes of the A0067 and the A0094 flat surfaces studied are ~ 1.3 and ~ 0.4 mm², respectively (Fig. 1, A and B). FE-SEM work showed that most of the A0067 flat surface is covered with a thin wrinkled phyllosilicate layer (Fig. 1C), which corresponds to the saponite-rich layer reported in (19), and the microcraters and the melt splashes formed on the thin layer. The A0094 flat surface lacks such a covering layer, and the CI chondrite-like Ryugu lithology is directly exposed to the surface. In some places, the A0094 flat surface shows a vesicular structure (Fig. 1D), which should correspond to the frothy layer previously reported on the surfaces of some small Ryugu particles (20). The frothy layer has been suggested to have formed by surface melting of regolith particles during frictional heating between loosely packed particles caused by meteoroid impacts (20). We found many Fe-Ni sulfide grains showing rough and concave grain surfaces on A0067 and A0094 flat surfaces (fig. S1). Similar surface-modified Fe-Ni sulfides have been reported on Itokawa and Ryugu regolith particle surfaces suggested to have suffered solar wind irradiation (23, 24). These features suggest that the A0067 and the A0094 flat surfaces were once exposed to space and suffered space weathering on the asteroid surface.

The microcraters on the flat surfaces are typically <1 μ m in diameter with a few up to 5 μ m (Fig. 1E) (20). Several dozen melt splashes were observed on the flat surfaces in this study. Most melt splashes are typically <5 μ m in size and consist mainly of silicate glasses. We found two remarkably large (>10 μ m) melt splashes, one from A0067 (Fig. 1, F and G) and the other from A0094 (Fig. 1H) (hereafter A0067-melt#1 and A0094-melt#1, respectively). A0067-melt#1 has a round shape and is ~ 20 μ m in diameter (Fig. 1F). It is composed of a glassy silicate main body and a smaller Fe-rich droplet (~ 10 μ m in diameter) on top (Fig. 1G). This droplet consists of small Fe-Ni metal grains (~ 200 to 300 nm in diameter) embedded in an Fe-Ni sulfide matrix (Fig. 1G). Small amounts of glassy splashes spread radially from A0067-melt#1 (Fig. 1F). A0094-melt#1 has an hourglass-like morphology and is ~ 15 μ m by 5 μ m in size (Fig. 1H). It contains numerous Fe-Ni sulfide inclusions and is probably made of two glassy silicate droplets connected to each other (I and II parts in Fig. 1H). Some cracked-shell-shaped melt splashes having similar surface texture with A0094-melt#1 were observed around A0094-melt#1 (Fig. 1H). In the present study, A0067-melt#1, A0094-melt#1, and one relatively large (~ 5 μ m in diameter) microcrater (hereafter A0067-crater#1; Fig. 1E) were subjected to microstructural and chemical analyses using XnCT and STEM-EDS. The present study deals with relatively large microcraters and melt splashes, and

description of typical small microcraters and melt splashes will be given in another paper.

A0067-melt#1

A0067-melt#1 and surroundings (~ 30 μ m-by- 30 μ m area) were extracted to the depth of ~ 20 μ m as a box-shaped sample using the focused ion beam (FIB) technique. The extracted sample was analyzed by XnCT to obtain the three-dimensional (3D) microstructure, and then a region of interest was extracted from the box-shaped sample as a thin section by FIB and analyzed by STEM-EDS. This analysis revealed that the glassy silicate in A0067-melt#1 has a smooth boundary with the attached Fe-rich droplet (Figs. 2 and 3, A to C). One large void (~ 7 μ m in diameter; Fig. 2) and small Fe-rich spherules (<100 nm in diameter; Fig. 3, A to C) were observed in the silicate glass. Most of the spherules have an Fe-Ni metal core and Fe-Ni sulfide mantle (Fig. 3D).

The glassy silicate has a homogeneous Mg-Fe-rich composition (Fig. 3, A and B) with the atomic ratio Mg/(Mg + Fe) (hereafter Mg#) of ~ 0.65 (table S1). The major element composition is plotted in Fig. 4A around an extension of a line connecting the bulk CI chondrite composition (25) and the Fe vertex in a [silicon (Si) + aluminum (Al)]–Mg–Fe ternary diagram (hereafter CI–Fe line). The other elements included in the glassy silicate are sulfur (S), calcium (Ca), and chromium (Cr) [0.4 to 1.8 atomic % (at %); fig. S2, A to C, and table S1]. The glassy silicate shows oxygen (O) deficiency if we assume simple oxide composition for each cation species (fig. S3 and table S1). The deficient O is estimated to be -10.2 at % if we assume Fe²⁺ as the valence of Fe in the glass (table S1). The oxygen to cations ratio correcting for S-bonded Fe and Ni [atomic ratio O/(cations – S)], is calculated to be ~ 1.2 , which is comparable to those of the frothy, highly dehydrated layers on the Ryugu sample surfaces (~ 1.2 to 1.3) (20).

The Fe-rich drop on the silicate glass surface (Fig. 1, F and G) shows a mottled texture in XnCT images (Fig. 2). It consists of dendritic crystals of α -(Fe-Ni) (~ 200 to 300 nm in diameter) embedded in an Fe-Ni sulfide matrix (Fig. 5, A and B). The number density of the dendritic crystal is high at the upper surface of the Fe-rich droplet (Fig. 3, A and B), and each of the crystal consists of a single α -(Fe-Ni) grain (Fig. 5, C and D). The Fe-Ni sulfide matrix consists mainly of troilite (Fig. 5, E and F), although the major Fe-sulfide phase in the Ryugu samples is pyrrhotite (19, 20), and contains small pentlandite grains (~ 50 nm in size; Fig. 5, A and B). The troilite and the pentlandite have a specific crystallographic relationship: $(001)_{\text{Tro}} // (11\bar{1})_{\text{Pen}}$ and $(010)_{\text{Tro}} // (101)_{\text{Pen}}$ (Fig. 5, G to I), and narrow gaps (<10 nm in width) parallel to troilite (001) plane were observed in the Fe-Ni sulfide matrix (Fig. 5, E and F). The bulk composition of the Fe-rich droplet is plotted at the point of Fe:Ni:S = $\sim 8.6:1:3.7$ within the Fe-troilite-pentlandite triangle in a S-Fe-Ni ternary diagram (fig. S4).

A0067-melt#1 is attached onto the saponite-rich layer (~ 1 to 4 μ m in thickness) lying on the A0067 main body (Figs. 2 and 3A). A few cone-shaped pores (~ 1 to 2 μ m in size) were observed at the boundary of A0067-melt#1 and the saponite-rich layer (Figs. 2 and 3A). A thin Si-rich layer (<100 nm in thickness) occurs on the upper surface of the saponite-rich layer (Fig. 3, A and B). It is uncertain whether this layer is crystalline or amorphous. The saponite-rich layer mainly consists of well-crystallized Mg-rich saponite and serpentine (Mg# ~ 0.81 ;

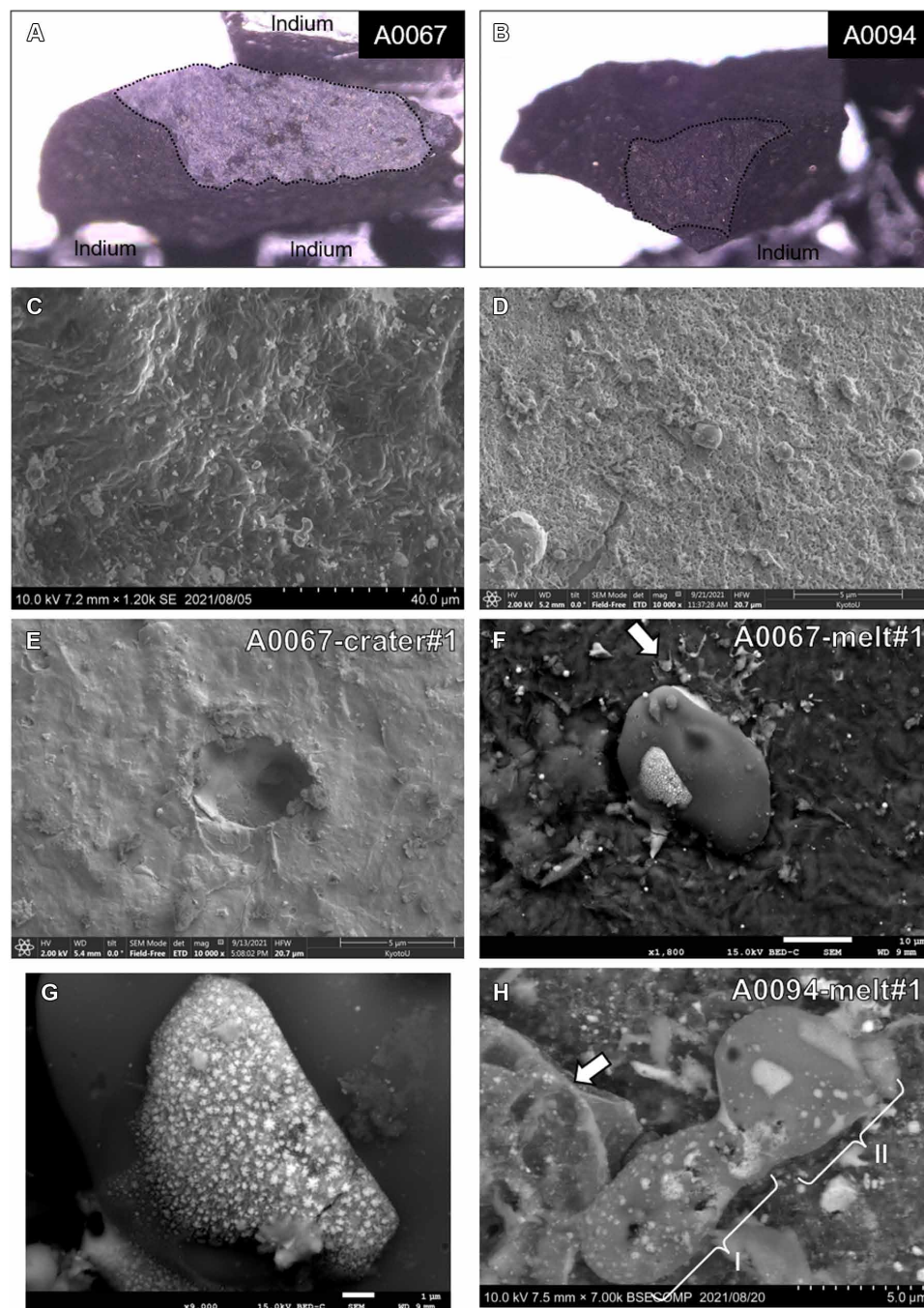


Fig. 1. Optical microscope and SEM images of the flat surfaces of A0067 and A0094 particles. (A and B) Optical microscope images of the A0067 and the A0094 flat surfaces (indicated by black dotted lines). The particles are held by indium. (C) Secondary electron (SE) image of wrinkled phyllosilicate layer covering the A0067 flat surface. (D) SE image of the A0094 flat surface showing vesicular structure. (E) SE image of A0067-crater#1. (F) Back scattered electron (BSE) image of A0067-melt#1 consisting of a silicate glass main body and an attached Fe-rich droplet. Splashes of glassy material spreading radially from A0067-melt#1 are indicated by a white arrow. (G) BSE image of the Fe-rich droplet splashed onto the silicate glass main body. (H) BSE image of A0094-melt#1 consisting of two glassy silicate droplets attached to each other (I and II parts). A0094-melt#1 containing abundant Fe-Ni sulfides (bright grains). Cracked-shell-shaped melt splashes occurring nearby A0094-melt#1 are indicated by a white arrow.

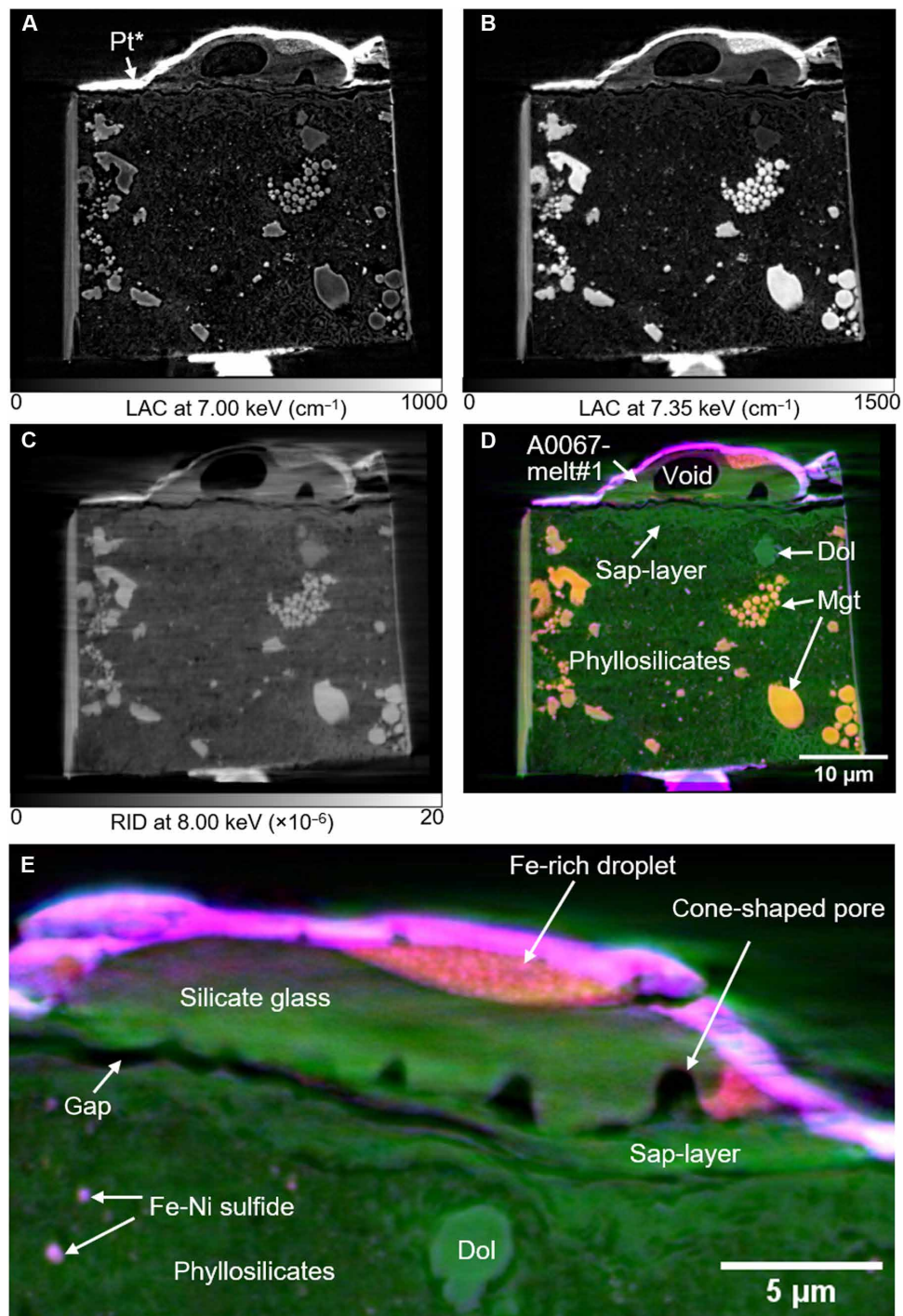


Fig. 2. XnCT images of A0067-melt#1. (A and B) Absorption and (C) phase shift XnCT images of A0067-melt#1 taken at 7, 7.35, and 8 keV, respectively. (D) Color-merged image of the three types of images (red: LAC, 0 to 1500 cm^{-1} at 7.35 keV; green: RID, 0×10^{-6} to 20×10^{-6} at 8 keV; blue: LAC, 0 to 1000 cm^{-1} at 7 keV). A0067-melt#1 contains a large void and is attached to the saponite-rich layer (Sap-layer) covering the A0067 main body (E) Magnified image of A0067-melt#1 in another slice of the color merged XnCT image. The slice was subjected to TEM analysis (see Fig. 3). A0067-melt#1 consisting mainly of glassy silicate and an Fe-rich droplet with a mottled texture. A few cone-shaped pores are recognized at the boundary between A0067-melt#1 and the saponite-rich layer. Stripe noise and unevenness in contrast of the glassy silicate are lighting artifacts. Mgt, magnetite; Dol, dolomite; Pt*, Pt deposition formed during the FIB sample processing.

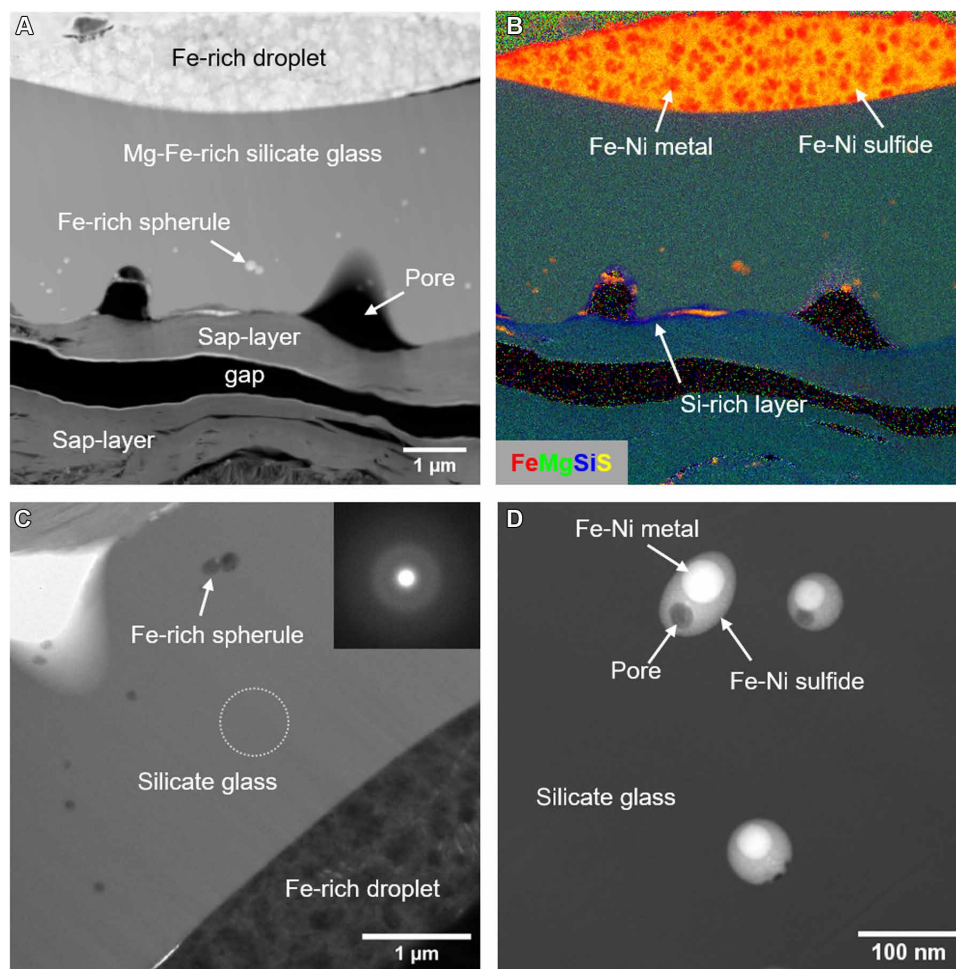


Fig. 3. TEM and STEM images of A0067-melt#1. (A and B) High-angle annular dark field (HAADF) STEM image and a combined elemental map for Fe (red), Mg (green), Si (blue), and S (yellow) of A0067-melt#1. A0067-melt#1 is attached to the saponite-rich layer covering the A0067 main body. A thin Si-rich layer is observed on the surface of the saponite-rich layer. (C) Bright-field (BF) TEM image of the silicate glass in A0067-melt#1. Inset is the SAED pattern of the silicate glass obtained from the circled area. (D) HAADF-STEM image of the Fe-rich spherules in the silicate glass. The spherules have a core-mantle structure with Fe-Ni metal core and Fe-Ni sulfide mantle.

Fig. 4A and table S2) and contains minor amounts of sodium (Na: 1.1 to 1.6 at %; table S2 and fig. S2D). The phyllosilicate sheets are developed along with the surface of the A0067 main body (fig. S5, A and B). Some gaps (<1 μm in width) occasionally occur between the phyllosilicate sheets (fig. S5, A and B). The A0067 main body, lying under the saponite-rich layer, consists mainly of Mg-rich phyllosilicate, Fe-Ni sulfides, magnetite, and carbonates (Fig. 2 and fig. S5, C to F). The mineralogy is consistent with CI chondrite-like Ryugu's major lithology (18–22, 26, 27).

A0094-melt#1

A0094-melt#1 and the surroundings (~20 μm-by-20 μm area) were extracted to the depth of ~20 μm as a box-shaped sample and analyzed by XnCT and TEM in a similar way to A0067-melt#1. A0094-melt#1 is directly attached to the A0094 main body (Fig. 6) with narrow gaps (~300 nm in width) occasionally occurring at the boundary (Fig. 7A). A thin Si-rich layer was observed on the surface of the A0094 main body (Fig. 7, A and B). A0094-melt#1 is

compositionally inhomogeneous and shows patchy structure with Fe-rich and Fe-poor glassy silicate regions (2 to 5 μm in diameter; Figs. 6 and 7, A to C). The boundaries between the Fe-rich and the Fe-poor regions are unclear (Figs. 6 and 7, A to C). The I and the II parts in A0094 melt#1 (see Fig. 1H) are largely occupied by the Fe-poor and the Fe-rich regions, respectively (Fig. 6). Spherical voids (a few tens of nanometers to ~2 μm in diameter) are abundant both in the Fe-rich and the Fe-poor regions (Figs. 6 and 7A). Coarse-grained Fe-Ni sulfides (~200 to 500 nm in diameter) are present on the upper surface of A0094-melt#1 (Fig. 7C). These correspond to Fe-Ni sulfide inclusions observed on the A0094-melt#1 surface by FE-SEM (see Fig. 1H). One of those was identified as troilite based on a selected-area electron diffraction (SAED) pattern (fig. S6). As the Fe-Ni sulfides show high atomic ratios (Fe + Ni)/S (up to ~2.4), some small Fe-Ni metal phase might occur inside the sulfide grains.

We found one Fe-poor region and two Fe-rich regions (#1 and #2 in Fig. 7C) in the TEM section. The Fe-poor region contains almost no crystalline phase. The two Fe-rich region show similar characteristics and contain abundant Fe-Ni sulfides (<500 nm in diameter).

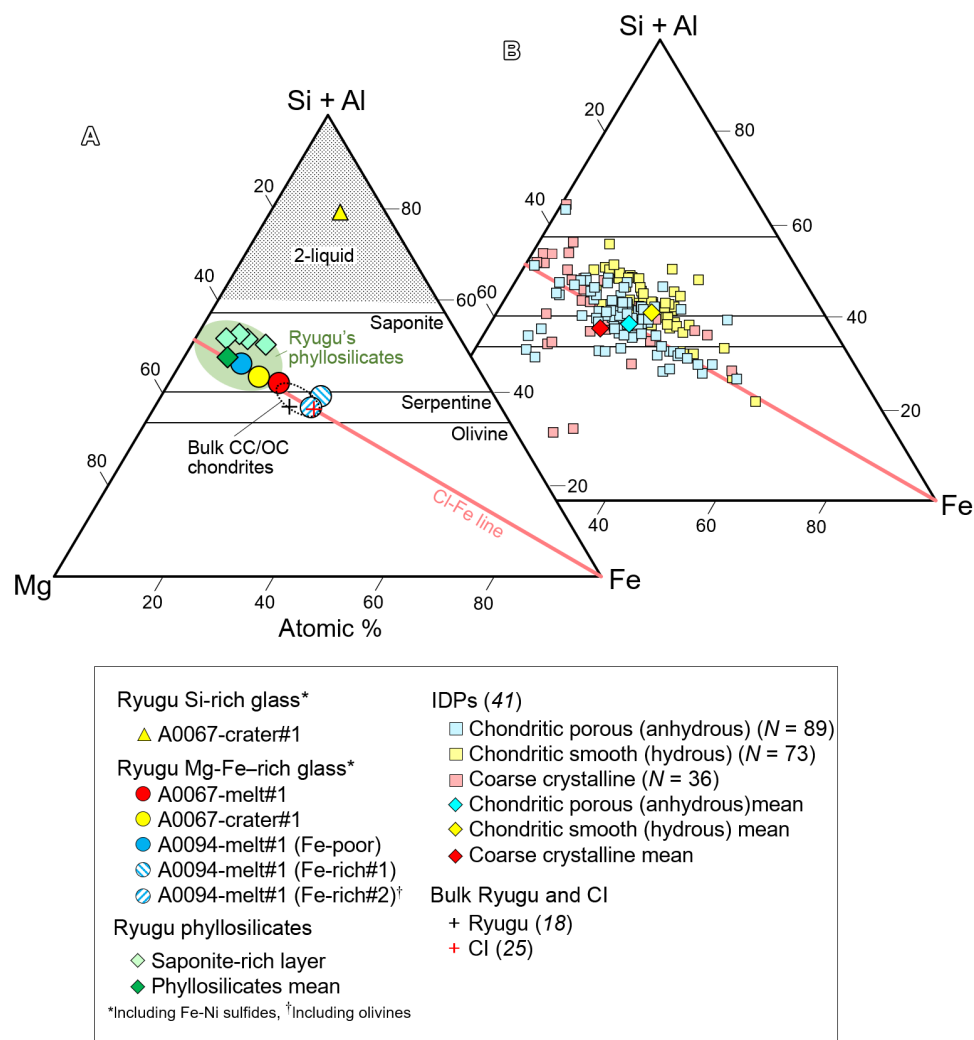


Fig. 4. (Si + Al)-Mg-Fe atomic % ternary diagram of compositions of the melt splashes. (A) Major element compositions of the melt splashes studied and **(B)** those of IDPs. The compositions are plotted along with an extension of a line combining the bulk CI chondrite composition (25) and Fe vertex (CI-Fe line). The compositions of the saponite-rich layer are also plotted. The compositions of IDPs are from (41), Ryugu's bulk composition is from (18), and the representative composition of the phyllosilicates in the Ryugu major lithology is from (19). The compositional field of Ryugu phyllosilicates (774 analyses) (19) is shown as a green colored oval, while that of bulk ordinary and carbonaceous chondrites (OC and CC, respectively) is indicated by a black open oval. The hatched area indicates the two liquid field in the MgO-FeO-SiO₂ system (58).

Most of the Fe-Ni sulfides have spherical to roundish shapes (Fig. 7D), while some of those in the Fe-rich region#1 show angular shapes (Fig. 7E). Some of the Fe-Ni sulfides show high atomic ratios (Fe + Ni)/S like as those on A0094-melt#1 surface (Fig. 7, A and B). We found two olivine grains (1 to 2 μm in diameter) in Fe-rich region#2 (Fig. 7, F to H). One of these is located at the bottom of A0094-melt#1 (olivine#1 in Fig. 7B) and contains abundant voids and Fe-Ni sulfide inclusions (<200 nm in diameter) (Fig. 7G). The other olivine also contains voids and Fe-Ni sulfide inclusions and is present at the upper surface of A0094-melt#1 (olivine#2 in Fig. 7B). Olivine#2 consists of domains elongated along crystallographic *b* axis (Fig. 7H). The *b* axis direction is normal to the A0094-melt upper surface. As the olivine grains are small in size and contain abundant voids and Fe-Ni sulfide inclusions, their compositions could not be measured. No solar flare track was observed in the olivine grains though the abundant voids and inclusions might have

made it difficult to recognize small tracks if present. Each olivine grain is surrounded by a thin glassy silicate layer (<100 nm in thickness) enriched in Fe compared to the surrounding silicate glass (Fig. 7, A to C). In addition, we found some carbonaceous aggregates (0.3 to 1 μm in diameter) consisting mainly of spongy carbonaceous material, irregular-shaped Fe-Ni sulfides, and Mg-rich silicates in A0094-melt#1 (Fig. 7I and fig. S7). The carbonaceous material is depleted in O and nitrogen (N) and expected to be inorganic carbon (C) (fig. S7). SAED of the carbonaceous material exhibits a ring pattern with broad peaks at ~ 0.21 and ~ 0.12 nm (Fig. 7I), indicating generally low crystallinity and the possible presence of turbostratic-graphite or nanodiamond grains (28–30).

The major element compositions of the Fe-poor and the Fe-rich regions (table S1), including Fe-Ni sulfides and olivine, are plotted in Fig. 4A along with the CI-Fe line in a (Si + Al)-Fe-Mg ternary diagram. The Fe-poor region shows high Mg# (~ 0.79) compared to

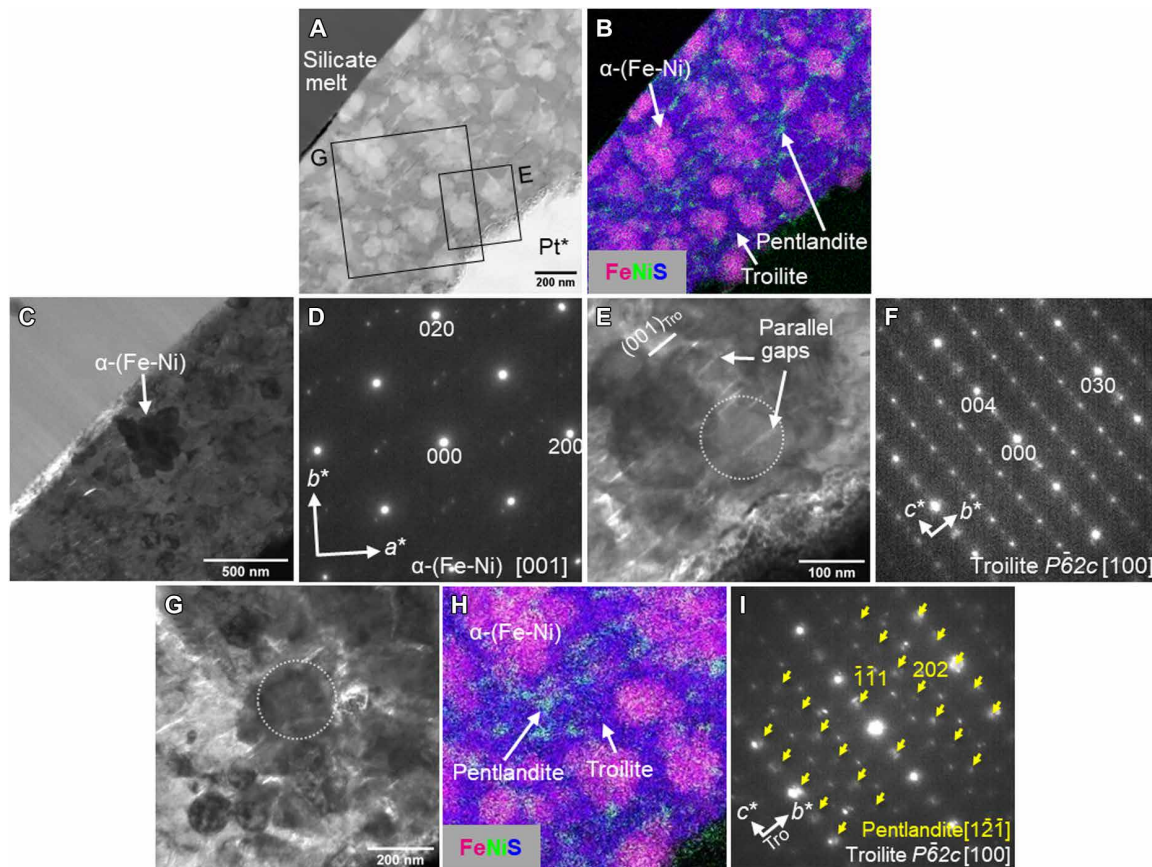


Fig. 5. TEM and STEM images of an iron-rich opaque droplet in A0067-melt#1. (A and B) HAADF-STEM image and a combined elemental map for Fe (magenta), Ni (green), and S (blue) of the Fe-rich droplet. (C) BF-TEM image of an α -(Fe-Ni) crystal. (D) SAED pattern obtained from the α -(Fe-Ni) in (C). (E) BF-TEM image of the rectangular E area in (A). SAED pattern obtained from the circled area is shown in (F). Narrow gaps parallel to the (001) troilite plane are recognized in the troilite matrix. (G and H) BF-TEM image and a combined elemental map for Fe (magenta), Ni (green), and S (blue) in the rectangular G area in (A). SAED pattern obtained from the circled area is shown in (I). The SAED pattern indicates that pentlandite has a specific crystallographic relationship with the troilite: $(001)_{\text{Tro}} // (11\bar{1})_{\text{Pen}}$ and $(010)_{\text{Tro}} // (101)_{\text{Pen}}$.

the Fe-rich regions (~ 0.52 and 0.55 for Fe-rich regions #1 and #2, respectively; Fig. 4A and table S1). The Fe-poor and the Fe-rich regions contain different amounts of Fe-Ni sulfides; however, this is not the main cause of the Mg# variation as the Fe contents have no clear correlation with the S contents (table S1 and fig. S2A). The major element composition of the Fe-poor region is similar to the Ryugu's phyllosilicates, while those of the Fe-rich regions are similar to the bulk CI chondrite composition (Fig. 4A) (25). We performed Fe L_3 -edge EELS analyses of the glassy silicates in the Fe-poor and the Fe-rich regions. The Fe L_3 -edge EELS spectra of the Fe-rich and the Fe-poor regions peak at ~ 707.8 and ~ 709.0 eV, respectively (fig. S8). Both peaks are positioned at lower energy side than that of the underlying phyllosilicates (~ 709.2 eV; fig. S8), showing that the glassy silicates have more reduced Fe states compared to the phyllosilicates. The Fe-poor region contains minor amounts of Na (1.3 at %) besides the major elements (table S1 and fig. S2D). The Fe-rich regions show relatively high concentrations of S and Ni (2.0 to 4.9 at % and 0.6 to 1.4 at %, respectively; table S1 and fig. S2, A and E) and contain minor amounts of Na, Ca, and Cr (0.4 to 1.5 at %; table S1 and fig. S2, B to D). The Fe-rich region#1 is slightly enriched in S and Ni compared to the Fe-rich region#2 (table S1 and fig. S2, A and E). Both the Fe-poor and the Fe-rich regions show O deficiency in similar degrees with the glassy silicate in A0067-melt#1 (-14.0 to

-10.4 at % if we assume Fe^{2+} as the valence of Fe in the glass; fig. S3 and table S1). The atomic ratio $\text{O}/(\text{cations} - \text{S})$ of the Fe-poor and the Fe-rich regions (~ 1.0 to 1.2) are comparable to slightly lower than that of the glassy silicate in A0067-melt#1. A0094-melt#1 contains some amounts of C mostly in the carbonaceous aggregates. However, the exact C content could not be obtained.

A0067-crater#1

A0067-crater#1 and adjacent area ($\sim 15 \mu\text{m}$ —by— $15 \mu\text{m}$ area) were extracted to the depth of $\sim 20 \mu\text{m}$ as a box-shaped sample and analyzed by XnCT and STEM-EDS. The analyses revealed that A0067-crater#1 is $\sim 4 \mu\text{m}$ in depth and intrudes the saponite-rich layer at surface of the A0067 main body (Figs. 8 and 9, A and B). The saponite-rich layer follows the crater wall with some gaps (up to 500 nm in width) between the phyllosilicate sheets (fig. S9, A to C). The saponite-rich layer becomes thinner ($< 1 \mu\text{m}$ in width) and compact just under A0067-crater#1 (fig. S9D). Beneath the saponite-rich layer, the A0067 main body consists of the CI chondrite-like Ryugu major lithology (Fig. 8).

A small amount of mixed glassy silicates and Fe-Ni sulfides is trapped on the wall of A0067-crater#1 (Figs. 8 and 9), with a layered flow structure (30 to 250 nm in thickness) developed along with the well-crystallized, saponite-rich crater wall (Fig. 9, A to C). The glassy

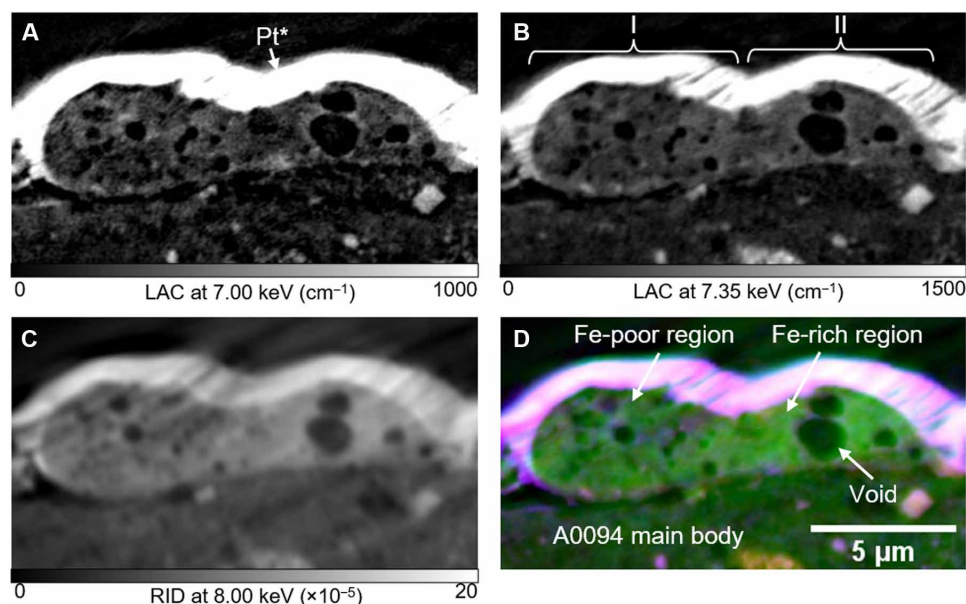


Fig. 6. XnCT images of A0094-melt#1. (A and B) Absorption and (C) phase shift XnCT images of A0094-melt#1 taken at 7, 7.35, and 8 keV, respectively. (D) Color merged image of the three types of images (red: LAC, 0 to 1500 cm^{-1} at 7.35 keV; green: RID, 0×10^{-6} to 20×10^{-6} at 8 keV; blue: LAC, 0 to 1000 cm^{-1} at 7 keV). A0094-melt#1 contains numerous voids and is attached directly to the A0094 main body. A0094-melt#1 consists mainly of glassy silicate and shows a patchy structure with Fe-rich and Fe-poor regions (the bright and the dark regions in the XnCT images). The boundary between the two regions is unclear. The I and the II parts of A0094-melt#1 (compare Figs. 1H and 6B) largely consist of the Fe-poor and the Fe-rich regions, respectively. TEM analysis was performed on the slice shown in this figure (see Fig. 7).

silicate is compositionally inhomogeneous and separated into Mg-Fe-rich and Si-rich zones (Fig. 9, A and B) with clear boundaries (fig. S10). The Si-rich glass is less abundant than the Mg-Fe-rich glass (Fig. 9, A and B) and selectively occurs along with the crater wall (Fig. 9D). Spherical voids (<200 nm in diameter) are abundant both in the Mg-Fe-rich and the Si-rich glasses (Fig. 9, D to F). Small Fe-Ni sulfide spherules (<100 nm in diameter) are abundant in the Mg-Fe-rich glass and less abundant in the Si-rich glass (Fig. 9, D to F). Some of the Fe-Ni sulfide spherules are present on the surfaces of the spherical voids (Fig. 9E).

The major element composition of the Mg-Fe-rich glass (Mg# ~0.72) is plotted in Fig. 4A along with an extension of the CI-Fe line in a (Si + Al)-Fe-Mg ternary diagram (Fig. 4A and table S1). The other elements included in the Mg-Fe-rich glass are Na, S, Ca, and Ni [0.2 to 1.9 at %; fig. S2 (A, B, D, and E) and table S1]. The Mg-Fe-rich glass shows O deficiency as for those in the A0067-melt#1 and the A0094-melt#1 (−7.4 at % if we assume Fe^{2+} as the valence of Fe in the glass; fig. S3 and table S1). The atomic ratio O/(cations − S) (~1.2) is as same as those of the glassy silicates in A0067-melt#1 and A0094-melt#1. The Si-rich glass has a very silica-rich composition [atomic ratio Si/(Mg + Al + Si + Fe) = ~0.69 and Mg# ~0.39; Fig. 4A and table S1] and contains minor amounts of Na, S, and Ni [0.9 to 2.6 at %; fig. S2 (A, D, and E) and table S1]. The Si-rich glass does not show O deficiency unlike the Mg-Fe-rich glass (fig. S3 and table S1).

The Fe-Ni sulfide layer is composed of small troilite grains (~200 to 500 nm in diameter) and contains no voids (Fig. 9, D and E). Some small (<200 nm in diameter) carbonaceous aggregates texturally similar to those in A0094-melt#1 occur around the troilite (Fig. 9, D and E). As the troilite grains show high (Fe + Ni)/S atomic ratios (~1.7 to 1.9), some small Fe-Ni metal phase probably occur inside the grains and one Fe-Ni metal spherule (~100 nm in diameter) was found in a troilite grain (Fig. 9G). Amorphous and vesicular Fe

oxide was commonly observed at the boundary between the Fe-Ni sulfide layer and the saponite-rich layer (Fig. 9, A, B, and H). The saponite-rich layer is poorly crystalline adjacent to the Fe oxide (Fig. 9H). The crater filling material contains minor amounts of C mostly in the carbonaceous aggregates although quantitative data are lacking.

DISCUSSION

Situation where the microcraters and the impact melt splashes formed

Previous studies revealed that Ryugu formed from a larger parent body formed at the outer Solar System beyond the CO_2 snow line [>3 to 4 astronomical units (au) from the sun] 1.8 to 2.9 million years (Ma) after the Ca-Al-rich inclusions (the oldest solids in the Solar System) (12, 14, 19). Ryugu's parent body was scattered into the inner Solar System after formation and subsequently disrupted by a large-scale impact event. The impact fragments were subsequently accreted to form the second-generation asteroids probably corresponding to the Eulalia or the Polana asteroid family in the asteroid belt (13, 14, 31, 32), of which Ryugu is probably a member (14, 31).

Ryugu should have experienced some degree of regolith resurfacing (33). Okazaki *et al.* (34) estimated cosmic ray exposure age of Ryugu samples to be ~5 Ma. As the average resurfacing time of the top ~1-m layer of Ryugu has been estimated to be longer at the near-Earth region (~2 to 8 Ma) than at the asteroid belt (<1 Ma), the relatively long sample exposure age suggests residence at the near-Earth region (1 au from the sun) for several Ma (14, 33, 34). This further suggests that the microcrater and the melt splashes reported here probably formed during Ryugu's residence in a near-Earth orbit within the last ~5 Ma.

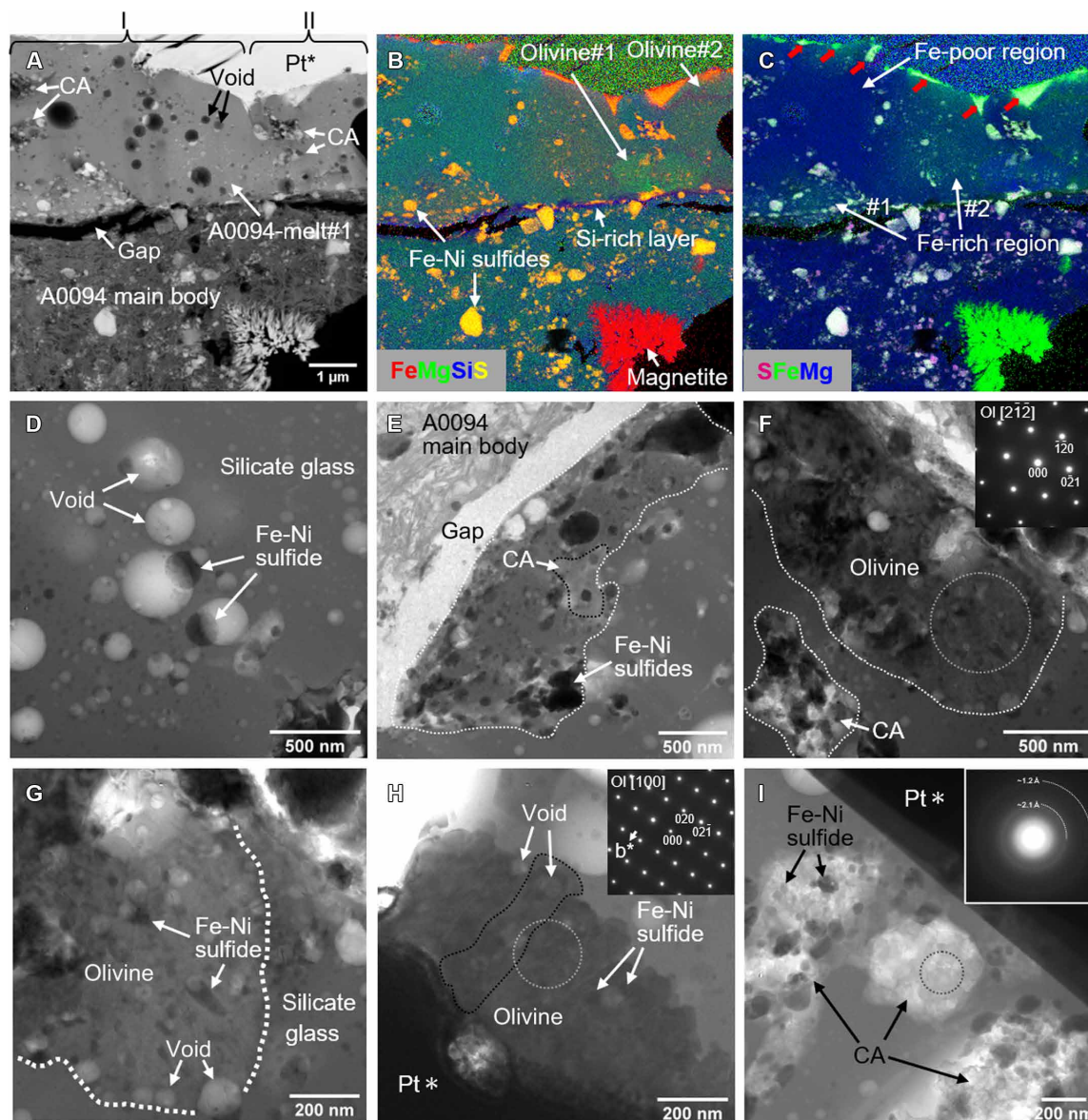


Fig. 7. TEM and STEM images of A0094-melt#1. (A to C) HAADF-STEM image and combined elemental maps for Fe (red), Mg (green), Si (blue), and S (yellow) and for S (magenta), Fe (green), and Mg (blue) of A0094-melt#1 attached onto the A0094 main body, respectively. Some large Fe-Ni sulfide grains formed on the upper surface of A0094-melt#1 [indicated by red arrows in (C)]. A0094-melt#1 is separated into Fe-rich and the Fe-poor regions. Two Fe-rich regions (#1 and #2) are recognized in the TEM section. A thin Si-rich layer is observed on the surface of the A0094 main body. The Fe-Ni sulfides in A0094-melt#1 show higher Fe/S atomic ratios and appear redder in (B) compared to those in the A0094 main body. (D) BF-TEM image of voids and Fe-Ni sulfide spherules in A0094-melt#1. (E) BF-TEM image of the Fe-rich region with irregular-shaped Fe-Ni sulfides (indicated by white dotted lines). (F to H) BF-TEM images of olivine#1 and #2 grains in the Fe-rich region. The insets are SAED patterns obtained from the circled areas in the olivines. Olivine#1 in (F and G) contains abundant voids and Fe-Ni sulfide inclusions. Olivine#2 in (H) consists of domains elongated along the crystallographic *b* axis. One of these domains is indicated by a black dotted line. (I) BF-TEM image of carbonaceous aggregates (CA) consisting of spongy carbonaceous material, irregular-shaped Fe-Ni sulfides, and Mg-rich amorphous silicates. The inset is a SAED pattern obtained from the carbonaceous material dominant portion (circled area).

Micrometeoroids tend to have high impact velocities at the near-Earth region compared to those at the asteroid belt. On the Moon, micrometeoroids are suggested to have a broad impact velocity distribution with a peak at ~ 9 km/s, whereas those on Earth have a sharp distribution with a peak at a slightly higher velocity of ~ 11 km/s (35). This is because the moon has a lower gravity force and thus makes lesser gravitational focusing

effects on micrometeoroids compared to Earth (35). Micrometeoroids hitting Ryugu are then expected to have a broad impact velocity distribution with a peak at a lower velocity than the moon. Among those, high-velocity micrometeoroid impacts might cause complete vaporization of the impactors. In this case, the target Ryugu surface would also suffer substantial vaporization, and the residual impact melts would have compositions

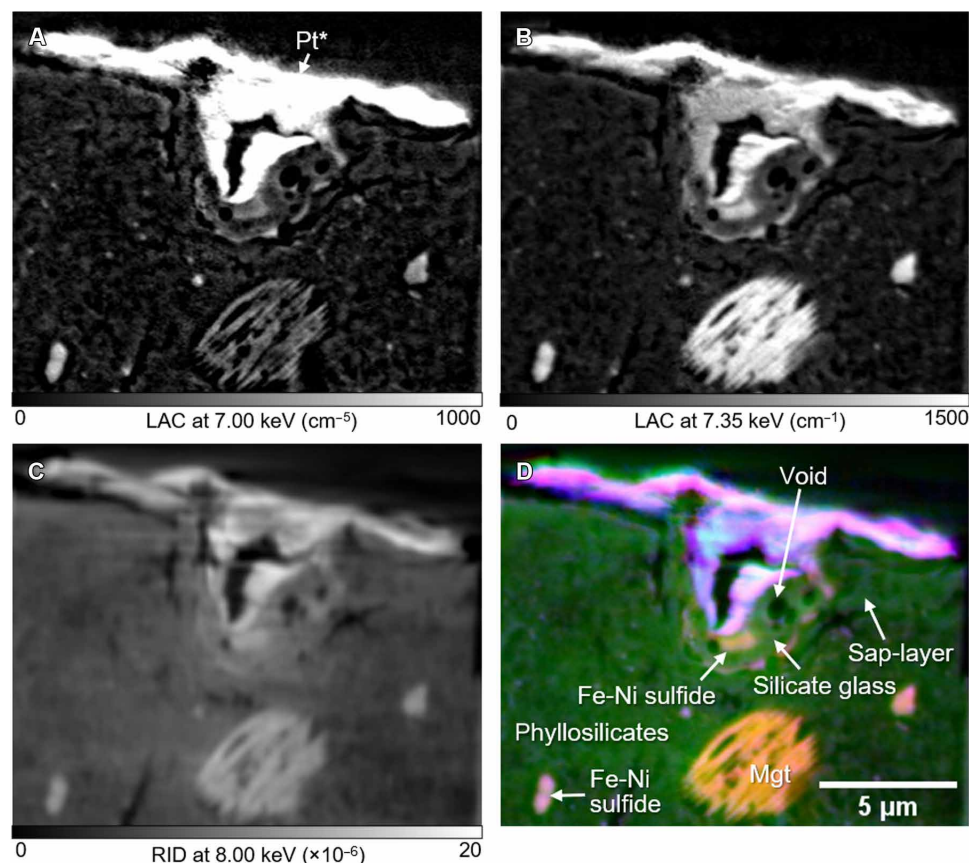


Fig. 8. XnCT images of A0067-crater#1. (A and B) Absorption and (C) phase shift XnCT images of A0067-crater#1 taken at 7, 7.35, and 8 keV, respectively. (D) Color merged image of the three types of images (red: LAC, 0 to 1500 cm^{-1} at 7.35 keV; green: RID, 0 to 20×10^{-6} at 8 keV; blue: LAC, 0 to 1000 cm^{-1} at 7 keV). A0067-crater#1 intrudes into the saponite-rich-layer and shows a tapered structure. A mixture of glassy silicate and Fe-Ni sulfide is trapped on the crater wall. The A0067 main body under the saponite-rich layer contains plaquette magnetite (Mgt) and Fe-Ni sulfides embedded in the phyllosilicate matrix.

showing elemental fractionations caused by the vaporizations. As the impact melts studied show no apparent depletion of volatile elements other than O and S (fig. S11), the actual impact velocities are expected to be not so high. In this case, major parts of the impactors and the Ryugu surface materials would be retained on the asteroid surface other than highly volatile components, and the impact melts studied would have compositions that are mostly explained by mixing of the impactors and the Ryugu surface materials. In the following, we discuss the nature of the source materials of the impact melts studied inferred from their compositions.

Source materials of the impact melts

The two impact melts studied and the A0067-crater filling material, which corresponds to an impact melt trapped in the crater, consist mainly of Mg-Fe-rich glassy silicates whose major element compositions lie along with the CI-Fe line with a wide range of Mg# (~0.52 to 0.79) in a (Si + Al)-Mg-Fe ternary diagram (Fig. 4A). Although the Mg-Fe-rich glassy silicates contain different amounts of small Fe-Ni sulfide inclusions, the main cause of the compositional variation is the compositional differences among the Mg-Fe-rich glassy silicates.

In the impact melts, the impactors and the Ryugu surface materials would have been mixed. A0094-melt#1 is compositionally

inhomogeneous and consists of Fe-poor and Fe-rich regions (Fig. 7, A to C) whose major element compositions are plotted at both ends of the compositional trend of the impact melts studied (Fig. 4A). This heterogeneity suggests an incomplete mixing of the source materials in A0094-melt#1, and the Fe-poor and the Fe-rich regions might be proximate to the original source materials. The studied impact melts show a single compositional trend (i.e., CI to Fe line), suggesting that they have common sources. The compositions of the source materials should be plotted along with the CI to Fe line. The Ryugu samples have for most elements a CI chondrite-like bulk composition (18, 19). This bulk composition and the compositions of Ryugu's major components, Mg-rich phyllosilicates, Fe-Ni sulfides, and magnetite (>90 vol % of the constituent minerals) (19) are plotted in Fig. 4A along with the CI-Fe line. Among those, Mg-rich phyllosilicates constitute more than 80 vol % of the Ryugu samples (except for large pores and cracks) (19), and micrometeoroid impacts on Ryugu could have caused dehydration of the Mg-rich phyllosilicates and formed melt mixtures of the Mg-rich phyllosilicates and coexisting nano-sized Fe-Ni sulfides (36). The representative composition of the Mg-rich phyllosilicates, which may include coexisting nano-sized Fe-Ni sulfides (19), is similar to the Fe-poor region in A0094-melt#1, the Mg-rich endmember of the impact melts studied (Fig. 4A). The Fe-poor region might have

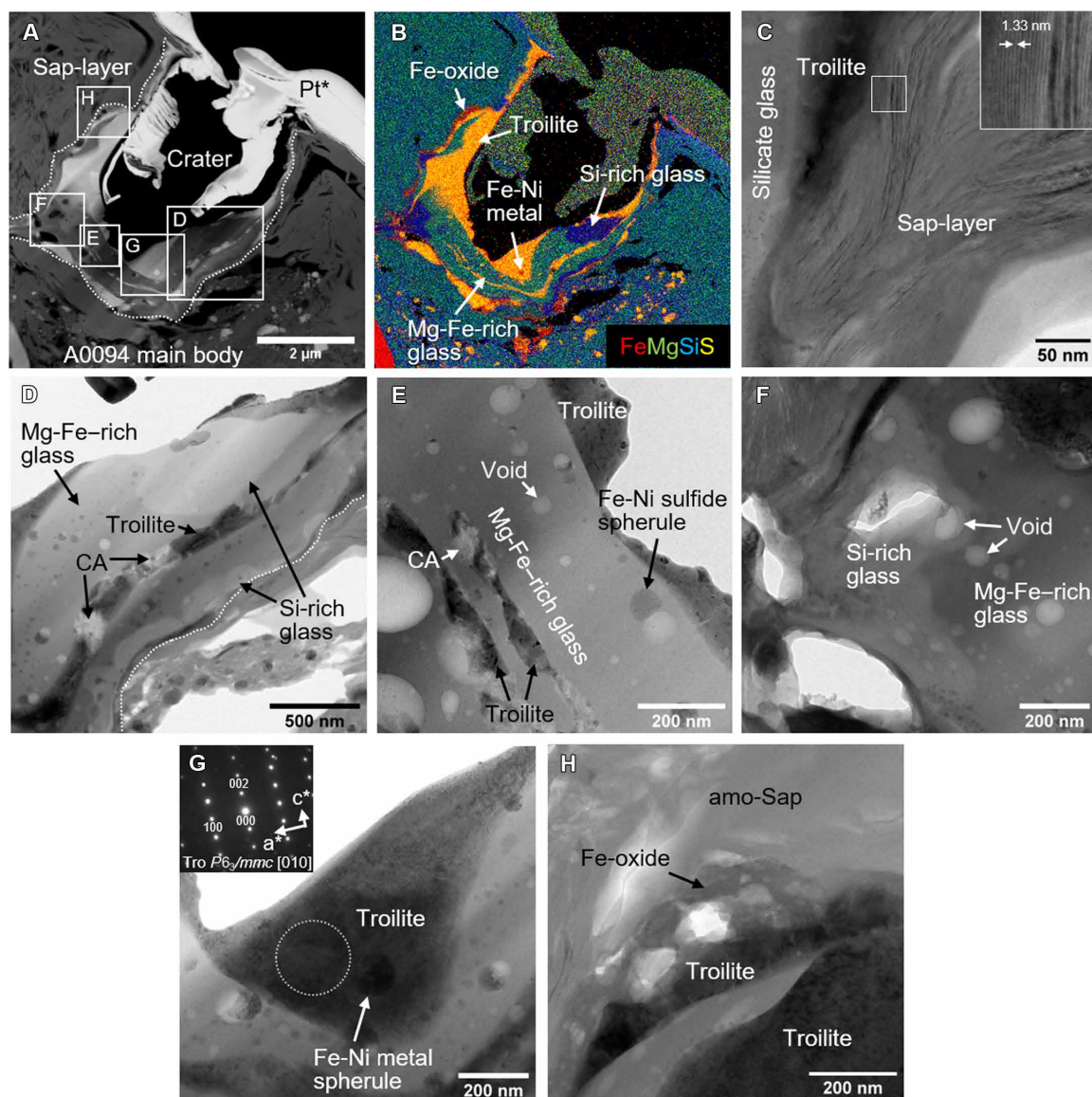


Fig. 9. TEM and STEM images of A0067-crater#1. (A and B) HAADF-STEM image and a combined elemental map for Fe (red), Mg (green), Si (blue), and S (yellow) of A0067-crater#1. A0067-crater#1 intrudes into the saponite-rich layer. The crater wall is indicated by white dotted lines in (A). A0067-crater#1 contains crater-filling material consisting of stacked glassy silicate and Fe-Ni sulfide layers. The glassy silicate is separated into Mg-Fe-rich and Si-rich parts. The Fe-Ni sulfides in A0067-crater#1 show higher Fe/S atomic ratios and are redder in (B) compared to those in the A0067 main body. (C) BF-TEM image of the boundary between the crater-filling material and the saponite-rich layer. The inset is an enlargement of the boxed area. The phyllosilicates constituting the saponite-rich layer are well crystallized. (D to F) BF-TEM image of the glassy silicates. The Si-rich glass occurs selectively along with the crater wall (indicated by a white dotted line). Small Fe-Ni spherules and voids are present both in the Mg-Fe-rich and Si-rich glasses. Small carbonaceous aggregates (CA) occur adjacent to the troilite grains composing the Fe-Ni sulfide layers. (G) BF-TEM image of a large troilite grain in the Fe-Ni sulfide layer. The troilite grain contains a small Fe-Ni metal spherule. The inset is a SAED pattern obtained from the circled area. (H) BF-TEM image of Fe oxide occurring at the boundary between troilite and the saponite-rich layer. Amorphous material with a saponite-like composition (amo-Sap) occurs around the boundary. Pt*, Pt deposition formed in the FIB sample processing.

sourced from the Mg-rich phyllosilicate matrix of Ryugu, and the matrix might be the source of the Mg-rich endmember.

The Fe-rich region#1 in A0094-melt#1 contains angular-shaped Fe-Ni sulfide grains (Fig. 7E). Fe-Ni sulfides could melt at relatively low temperatures (37, 38). Melted Fe-Ni sulfide typically show spherical to roundish shapes sometimes with flow structure governed by surface tension of liquid phases in silicate melts (39). The angular-shaped

Fe-Ni sulfide grains lack such morphology and probably escaped substantial melting and might correspond to relic sulfides originally contained in the source material. This suggests that A0094-melt#1 might have formed under a relatively low temperature. The presence of the relic Fe-Ni sulfides in A0094-melt#1 suggests that the Fe-rich regions went through insufficient melting and thus better preserve the original chemical and mineralogical characteristics of the source

material. The Fe-rich regions are small in size (2 to 5 μm ; Fig. 7, A to C) and show CI chondrite-like compositions (Fig. 4A), which deviate from the compositions of Ryugu's phyllosilicates and other fine-grained Ryugu components (Fig. 4A). This suggests that Ryugu is not the original source of the Fe-rich regions and that they were probably sourced from the impactors. Chondritic meteorites having CI chondrite-like bulk compositions (Fig. 4A) (25) cannot be the candidate for the impactor as they do not match with CI chondrite composition in size as small as the Fe-rich regions (40). The known small planetary materials having CI chondrite-like average compositions are interplanetary dust particles (IDPs) and micrometeorites derived from asteroids and comets (Fig. 4B) (41–43). Among those, anhydrous chondritic IDPs (typically 5 to 15 μm in size) (44, 45) show some variation in major element contents, which match well with the compositional range of the impact melts studied (Fig. 4B) (41). Anhydrous chondritic IDPs consists mainly of Mg-Fe-rich silicates, Fe-Ni metal and sulfides, and primitive organic materials and are suggested to have cometary origins (44–46). The mineralogy is broadly similar to the impact melts studied. Some primitive organic materials in anhydrous chondritic IDPs contain abundant mineral inclusions (mostly sulfides) (46) and are texturally similar to the carbonaceous aggregates in A0094-melt#1 (Fig. 7I). These primitive organic materials might be the precursor of the carbonaceous aggregates in A0094-melt#1. Although the carbonaceous aggregates in A0094-melt#1 are depleted in N and O unlike the primitive organic materials in anhydrous chondritic IDPs (fig. S7), the N and O originally contained in the precursor might have been lost from the carbonaceous aggregates during impact-induced heating. Matsumoto *et al.* (24) reported the presence of iron nitride on surfaces of some Ryugu particles, which formed via reduction of Fe-bearing minerals by solar wind irradiation and subsequent nitrification caused by interactions with N compounds in vapors produced by micrometeoroid impacts on the asteroid Ryugu surface. The N components originally contained in the carbonaceous aggregates in the present study might correspond to the source of these N compounds. From this line of evidence, we suggest that anhydrous chondritic IDPs are the plausible candidate for the impactors, which formed the impact melts studied, and that the Fe-rich regions and the carbonaceous aggregates in A0094-melt#1 correspond to the relict anhydrous chondritic IDPs impactors. We note that two olivine grains in Fe-rich region#2 (Fig. 7, F to H) are not the relicts of the impactor and should have crystallized in situ in A0094-melt#1. This is evident from the presence of Fe-rich glassy rims surrounding the olivine grains (Fig. 7B), a trace of Fe-Mg partitioning between liquid-solid phases during the crystallization. The voids and Fe-Ni sulfides within the olivine grains (Fig. 7, G and H) might have been captured during the crystallization.

The impact melts studied contain some minor elements (Na, S, Ca, Cr, and Ni; fig. S2, A to E, and table S1) in concentrations similar to those of Ryugu's phyllosilicates and anhydrous chondritic IDPs and can be explained by mixing of these materials (fig. S2, A to J) (25, 41). The S content variation is relatively large among the minor elements (fig. S2A and table S1), possibly reflecting not only the mixing of the source materials but also immiscible silicate-sulfide melt separation and sulfur losses during impact-induced heating as discussed below.

Cause of oxygen depletion of the impact melts

The impact melts studied are depleted in O compared to the bulk Ryugu samples and chondritic materials ($\text{O/Si} = \sim 0.5$ to $0.6 \times \text{Ryugu}$;

fig. S3 and table S1) (18, 19). This is probably partially due to H_2O losses from the melts during the impact-induced heating. The Fe L_3 -edge EELS analyses showed that A0094-melt#1 has more reduced state compared to the underlying phyllosilicate matrix (fig. S8). Although quantitative data were not obtained in the present study, the peak position and the half value width of the Fe L_3 -edge spectrum of the Fe-rich region in A0094-melt#1 are similar to those of the space-weathered Ryugu's surface layers having $\text{Fe}^{3+}/\Sigma\text{Fe}$ ratio of ~ 0.20 to 0.45 (20). The Fe-rich region might have a similar redox state with the space-weathered layers. Likewise, the underlying phyllosilicates might have a similar redox state with the Ryugu's phyllosilicates having $\text{Fe}^{3+}/\Sigma\text{Fe}$ ratio of ~ 0.85 to 0.95 (20). The Fe-poor region in A0094-melt#1 probably has an intermediate $\text{Fe}^{3+}/\Sigma\text{Fe}$ ratio between the Fe-rich region and the Ryugu's phyllosilicates. If the Fe^{3+} in the Ryugu's phyllosilicate matrix, which is one of the sources of the impact melts, was reduced to Fe^{2+} or more in the impact melt, then related oxygen losses would have occurred. This might also be responsible for the O depletion, although the oxygen losses estimated from the Fe contents in the melts are not so much. The other impact melts studied, which were not subject to EELS analysis, might have relatively reduced Fe state as they also show O depletion and might have experienced the Fe reduction. In addition, if the impact melts studied were sourced from the Ryugu and the impactors of CP-IDPs, then the source materials are expected to have contained substantial amounts of C mostly in organic materials and carbonates (18, 19, 41, 45). Although the exact C contents in the impact melts were not obtained in the present study, the absence of C in A0067-melt#1 and the low abundance of C-bearing material in the other melts suggest that substantial C losses occurred during the impact-induced heating, probably in the form of CO and CO_2 . This could have caused reduction of the remaining melts and might be responsible for the O depletion in the impact melts studied. If we assume that the original C content in the source materials was the same as those of bulk Ryugu and CP-IDPs ($\text{C/Si} = \sim 0.8$ and ~ 2.4 , respectively) (18, 19, 41) and that C was lost from the melts mainly as CO, then the corresponding O losses calculated from the Si contents in the melts are comparable to the O depletion in the impact melts studied (suggesting the original $\text{O/Si} = \sim 0.7$ to $1.0 \times \text{Ryugu}$) (18, 19).

As the impact melts studied show O deficiency compared to the simple oxide compositions, some metal phases are expected to occur in the impact melts. As shown by the present study, the impact melts probably have relatively reduced Fe state. However, even if we assume that all Fe and Ni in the impact melts are present as metallic Fe^0 and Ni^0 , this is insufficient to account for the entire O deficiency. This suggests the presence of another reduced phase in the impact melts. Previous studies (47, 48) performed repetitive ultraviolet laser pulse irradiation on amorphous SiO_2 in vacuum conditions (in the range 10^{-8} to 10^{-5} Pa) and reported generation of SiO_x ($x < 2$) (oxygen deficient-type defects) in the SiO_2 glass. These studies suggested generation of Si-Si bonding in SiO_4 tetrahedra network during the laser pulse flash heating and subsequent quenching of it. Loeffler *et al.* (48) also reported broadenings of Si-2p x-ray photoelectron spectrum peaks of Mg-rich olivines (Fo_{90} and Fo_{99+}) after the laser pulse irradiation, which may suggest reductions of Si in the olivines. We speculate that similar process might have occurred in the formation of the impact melts studied. Although the glassy silicates studied contain various cations and structurally differ from pure silicon-oxide glass and olivines, some oxygen deficient-type defects might have formed in the melt SiO_4 tetrahedra network

during the impact-induced flash heating, probably in association with the volatile losses. Subsequent quenching of the defects might have established the O deficiency in the impact melt studied.

Formation of homogeneous silicate glass and Fe-rich droplet in A0067-melt#1

The glassy silicate in A0067-melt#1 is texturally and compositionally homogeneous (Figs. 2 and 3). In A0067-melt#1, the melts derived from the impactor and the Ryugu surface material might have been thoroughly mixed each other. The glassy silicate contains almost no small voids unlike the other melt splashes. This implies that A0067-melt#1 went through a high degree of degassing among the impact melts studied, probably due to the high-temperature conditions of the impact-induced heating, and to the escaped volatiles. This is consistent with the low contents of volatile S and Na in the glassy silicate (fig. S2, A and D, and table S1). The A0067-melt#1 glassy silicate contains only minor amounts of Fe-Ni-rich metal-sulfide spherules and lacks other crystalline phases, which are expected to have crystallized from the melt when it attached on the A0067 surface. The lack of such a crystalline phase implies a highly viscous state for the glassy silicate at the time of attachment, probably due to supercooling. The attachment of the hot melt splash could have induced evaporation of volatiles from the saponite-rich layer (mostly H₂O). The gaps in the saponite-rich layer under A0067-melt#1 probably formed from shrinking of the phyllosilicate layers associated with the volatile losses (Fig. 3A). In the present study, we found cone-shaped pores formed between A0067-melt#1 and the saponite-rich layer (Figs. 2 and 3A), probably due to volatile escape. In addition, the large void in A0067-melt#1 (Fig. 2, A to D) may correspond to these volatiles captured in the melt before its solidification. The dehydration of the interlayer H₂O of saponite peaks at temperatures around ~90°C (18), and the temperature of the melt at the time of the attachment might be higher than this temperature. As the saponite-rich layer shows no evidence of decomposition to anhydrous silicates or notable amorphization, the temperature might have been <800°C (49).

A0067-melt#1 might have formed as a melt droplet of immiscible metal sulfide and silicate melts, which subsequently attached to the A0067 particle surface. The metal sulfide melt corresponds to the Fe-rich droplet splashing onto the glassy silicate (Fig. 1G). Upon melting, the metal-sulfide melt could have remained at the silicate melt surface, probably due to the low interfacial energy, and then become attached to the A0067 particle surface together with the silicate melt. Subsequently, a portion of the metal-sulfide melt should have flowed down the silicate melt surface before its solidification. The precursor of the Fe-rich droplet might have been the Fe-Ni sulfide grain(s) on Ryugu's surface or the impactor. Upon melting, some S should have volatilized and escaped from the Fe-Ni sulfide melt. The high concentration of Fe-Ni metal grains on the Fe-rich droplet surface (Fig. 3, A and B) is consistent with sulfur loss, which would have resulted in excess iron in the remaining melt. The dendritic Fe-Ni metal grains seem to have initially crystallized from the Fe-enriched melt (fig. S4). In general, cooling of a melt with the composition of the Fe-rich droplet would form a eutectic metal sulfide mixture (50, 51). The absence of a typical eutectic texture suggests that the Fe-rich droplet is formed by a nonequilibrium process due to rapid cooling. The rapid cooling could have induced formation of dendritic Fe-Ni metal crystals and might have prevented subsequent simultaneous crystallization of Fe-Ni metal and sulfide from the remaining melt (fig. S4). The Fe-Ni sulfide matrix should have crystallized from the residual melt with a composition around the FeS-(Fe,Ni)₉S₈ line in the S-Fe-Ni system

(fig. S4), and subsequent phase separation of FeS and (Fe,Ni)₉S₈ in the Fe-Ni sulfide matrix might have formed the present Fe-rich droplet (Fig. 5, A and B). If these hypotheses are true, then the composition of the precursor Fe-Ni sulfide(s) is speculated to be plotted around the intersection of the FeS-(Fe,Ni)₉S₈ line and the line connecting the S vertex and the bulk Fe-rich droplet composition in a S-Fe-Ni ternary diagram (fig. S4). The small Fe-Ni-rich spherules in the A0067-melt#1 glassy silicate, consisting of Fe-Ni metal core and Fe-Ni sulfide mantle (Fig. 3D), might have formed from similar S-depleted melt. The substantial sulfur loss supports the high-temperature conditions of the A0067-melt#1 forming impact.

Formation of the Mg-Fe-rich and Si-rich glassy silicates in A0067-crater#1

The small size of A0067-crater#1 is consistent with its formation by an impactor. The impactor diameter is estimated to be ~2 to 4 μm if we assume an impactor with a density of 1.0 to 5.0 g/cm³ (comparable to fluffy IDPs to dense mineral grains) and an impact velocity of ~6 km/s based on the previous experiments, which investigated a relation between projectile and crater sizes at the impact velocity using projectiles and targets with different densities (52–54). A bit of change in the impact velocity (in a range of ~1 to 9 km/s) might not cause substantial differences on the size estimation (54). The estimated impactor size is slightly smaller than typical IDPs. This small impactor still could have a CI chondrite-like composition as in the case of the Fe-rich regions in A0094-melt#1, or, alternatively, it might consist mainly of an individual mineral grain and have a composition deviated from those of typical sizes of IDPs. If we assume a cometary impactor, which is suggested to be common around a near-Earth region (55, 56), then the possible candidates for this mineral grain are Mg-Fe silicates and Fe sulfides, which dominate the small-size fractions of the 81P/Wild 2 comet samples collected in the Stardust mission (57). These are consistent with the mineralogy of the crater-filling material. As the crater-filling material contains abundant troilite grains, the impactor might have consisted mainly of Fe sulfide. In this case, the contribution of the impactor to the glassy silicate part of the crater-filling material should be small. This might be consistent with the major element composition of the glassy silicate, which is indicative of the large contribution of the Ryugu's phyllosilicates (Fig. 4).

The crater-filling material, deeply intruding the saponite-rich layer, should have formed in situ via impact-induced melting. The relatively high Na content in the crater-filling glassy silicate might be partially derived from the saponite-rich layer, which is enriched in Na compared to typical Ryugu phyllosilicates (fig. S2D). The impact melt trapped on the crater wall would have cooled faster than the melt splashed away from the crater due to heat dissipation to the periphery. The rapid cooling might have contributed to the preservation of volatile Na, originally contained in the source materials, in the glassy silicate. Melting of the saponite-rich layer and the A0067 main body would have induced degassing of volatiles (mainly H₂O in phyllosilicates) forming the voids in the glassy silicate (Fig. 9, D to F). The Fe oxide occurring at the boundary between troilite and the saponite-rich layer (Fig. 9H) probably formed by oxidation of the troilite by H₂O released from the surrounding phyllosilicates. As the entire impact melt shows a relatively reduced state and an Fe-Ni metal spherule is retained in the troilite (Fig. 9, B and G), the Fe-oxide formation would have

occurred during cooling after the impact melt mostly solidified and the oxidation effect should have been spatially localized probably due to the fast cooling.

The glassy silicate in the crater-filling material is separated into Mg-Fe-rich and the Si-rich glasses (Fig. 9, A and B). In general, melting of a silica-rich material produces immiscible Si-rich and -poor silicate liquids (58, 59). However, the low silica content in the Mg-Fe-rich glass is inconsistent with its formation through the immiscible melting of a silica-rich material (Fig. 4A). This means that the glassy silicates in the crater-filling material are not the products of the immiscible melting of a single silica-rich material. The Si-rich glass is less abundant compared to the Mg-Fe-rich glass and selectively occurs along with the crater wall (Fig. 9C), which suggests that the Si-rich glass formed in situ from a source material distributed on the crater wall. The phyllosilicates in the crater wall (saponite and serpentine) would decompose to pyroxene and olivine with silica glass at high temperatures ($>500^{\circ}$ and $>800^{\circ}\text{C}$ for serpentine and saponite, respectively) (49), and further heating would induce an incongruent melting of the pyroxene resulting in formation of olivine and a residual silica-rich melt (58, 60), if we assume a sufficient duration of heating. However, these seem not to be responsible for the formation of the Si-rich glass because the impact-induced abrupt heating and the subsequent rapid cooling would have prevented the phase separations of the precursor silicates. This prevention of incongruent melting of silicates due to an abrupt heating was previously reported in the 81P/Wild 2 comet impact recovery samples (39). In addition, the residual melt resulting from the incongruent melting of pyroxene generally have lower SiO_2 contents than the Si-rich glass in the present study (58). These suggest that some silica-rich material might have once existed on the surface of the saponite-rich layer and was involved in impact-induced heating to form the Si-rich glass. Melting of this Si-rich material could have formed immiscible Si-rich and Si-poor melts. The lack of such evidence in the Si-rich glass studied suggests that the rise in temperature was insufficient for the immiscible melting and only caused a deformation of the precursor Si-rich material probably around the glass transition temperature.

The presence of the silica-rich precursor on the Ryugu particle surfaces is expected from other respects. In the present study, we found thin Si-rich layers under A0067-melt#1 (Fig. 3B) and A0094-melt#1 (Fig. 7B), the candidates for the silica-rich material. The Si-rich layers should have been once exposed to space before the A0067-melt#1 and the A0094-melt#1 formed. Previous studies on Itokawa and lunar regolith samples reported the presence of thin amorphous layers on undisturbed sample surfaces (3, 7, 61) showing compositional variation, which probably formed by deposition of vaporized materials generated by solar wind irradiation and micrometeoroid impacts on the small bodies. In the case of the Ryugu, Si-rich vapor deposits are present (~ 10 nm in thickness) on some small Ryugu particles (20). We suggest that the Si-rich thin layers found in the present study may correspond to these vapor deposits formed on the Ryugu's surface, and the Si-rich glass in A0067-crater#1 represents the vapor deposits.

Implication for the origin of the impactors hit on the asteroid Ryugu

The present study examined impact melts formed by the impacts of micrometeoroids with chondritic compositions on Ryugu. The Fe-rich regions in A0094-melt#1, which are probably the relict fragments of the impactor, contain Mg-Fe-rich silicates, Fe-Ni sulfides, and carbonaceous materials. This mineralogy is similar to anhydrous

chondritic IDPs, which have been suggested to have cometary origin. The studied impact melts likely to have common sources and have formed by anhydrous chondritic IDP impacts on the Ryugu's surface. The impactors would have struck Ryugu while it was in a near-Earth orbit. Recent astronomical models suggested that most of the dust particles around a near-Earth region have cometary origins (55, 56) and are consistent with the present results. Further study of many more impact melt splashes and microcraters will give important information about the variation and flux of the impactors that hit on asteroid Ryugu and other near-Earth asteroids.

MATERIALS AND METHODS

Samples

A0067 and A0094 Ryugu particles returned from asteroid Ryugu by the Hayabusa2 spacecraft were subjected to analyses in the present study. The Ryugu particles were mounted on an indium plate with the flat surfaces faced upward.

FE-SEM observations and FIB microsampling

The flat sample surfaces were imaged using FE-SEM at Japan Aerospace Exploration Agency (JAXA) curation facility (Hitachi, SU6600). The uncoated samples were set into a sealed sample holder in the glove box purged with pure nitrogen. The sample holder was transported from the glove box to the FE-SEM without air exposure using a slow vacuum and purge system equipped with the FE-SEM. Observations were performed at a 10-kV accelerating voltage and 0.14- to 0.17-nA beam current under high- and low-vacuum conditions. After the FE-SEM observations, a thin Au coating (~ 5 nm in thickness) was applied to the flat sample surfaces. The Au-coated flat surfaces were observed by FE-SEM at Tohoku University (JEOL, JSM-7001F) operated at 15 kV and ~ 1.4 nA under high-vacuum condition.

Some microcraters and impact melt splashes on the flat sample surfaces were subjected to FIB microsampling to prepare box-shaped XnCT samples. The microsampling protocol has been described in detail in (62, 63). The microsampling was performed using an FIB system equipped with FE-SEM at Kyoto University (Thermo Fisher Scientific, Helios NanoLab G3 CX). In the FIB processing, we used a Ga^+ ion beam at a 30-kV accelerating voltage. Sample observation during the FIB processing was performed using an electron beam at a 2-kV accelerating voltage and ~ 0.09 -nA beam current. The box-shaped samples were extracted from the flat surfaces and mounted on tips of titanium (Ti) needles.

XnCT analysis

The box-shaped XnCT samples were analyzed by synchrotron radiation XnCT at SPring-8 BL47XU combining two methods—dual-energy tomography (DET) (64) and scanning imaging x-ray microscopy (SIXM) (65). These methods enable us to obtain nondestructive 3D nanostructures and mineralogy of micro-samples at high spatial resolution (66). In DET, we obtained 3D images with x-ray linear attenuation coefficients (LACs) at two energies—7 and 7.35 keV (voxel sizes: 47.17 and 49.44 nm, respectively)—below and above the k -absorption edge energy of iron (7.11 keV). The contrasts in the images at 7.35 keV strongly depend on iron contents, thus emphasizing iron-bearing minerals. In SIXM, we simultaneously obtained images of both x-ray absorption contrast with LACs and x-ray phase contrast with refractive index decrements (RIDs) at 8 keV (anisotropic voxel size: 111.06 nm by 111.06 nm by 108.1 nm). RID is simply the difference between the

refractive index and unity and is roughly proportional to the material density. After registration of the three types of XnCT images (LAC images at 7 and 7.35 keV and RID image), red-green-blue (RGB) color-merged images were made as mineral-phase maps in which we could distinguish mineral phase.

TEM and STEM-EDS analysis

After the XnCT analyses, a region of interest was extracted from each XnCT sample as a thin section (~100 to 200 nm in thickness) for TEM observations using FE-SEM-FIB systems at Kyoto University (Thermo Fisher Scientific, Helios NanoLab G3 CX) and at Tohoku University (Thermo Fisher Scientific, Versa 3D). For the extraction and the thinning treatment of TEM thin sections, we used a Ga⁺ ion beam at 30 kV. The damaged layers formed on thin sections during the thinning were removed using a Ga⁺ ion beam at 5 kV.

The thin sections were analyzed by STEM-EDS systems at Kyoto University (JEOL, JEM-2100F) and Tohoku University (JEOL, JEM-2100F) operated at 200 kV. TEM images were recorded using charge-coupled device (CCD) cameras (Gatan, Orius 200D) and then analyzed using the Gatan Digital Micrograph software package. Each mineral phase was identified on the basis of SAED patterns. We also acquired STEM images and x-ray elemental maps using the STEM-EDS systems and performed quantitative chemical analyses. Elemental maps containing x-ray intensities in individual pixels were acquired by scanning a focused electron beam ~10 to 30 pA at high speed (0.05 to 0.1 ms per point) multiple times. The elemental maps were deconvoluted, and image drifts were corrected for each scan frame. The x-ray intensities of individual elements were extracted from regions of interest in the maps and used for precise quantification. In the present study, O, Na, Mg, Al, Si, S, Ca, Cr, Fe, and Ni were subjected to the quantification. We excluded regions that show apparent of O x-ray absorption by Pt-coat layer from the quantification area. For quantification, we used the ζ -factor method (67). The ζ -factors of the instrument were determined for all elements of interest using a thin film of the National Institute of Standards and Technology Standard Reference Materials 2063a glass, according to protocols developed for the ζ -factor method (67). The CCD camera was used to measure the accurate electron beam current required for the quantification.

We performed qualitative EELS analyses only for A0094-melt#1 due to a sample availability. The EELS analyses were performed using a JEOL monochromated JEM-ARM200F at the Institute for Chemical Research, Kyoto University. This microscope has a monochromator, an aberration corrector for STEM (CEOS), an EDX system (JED-2300 T silicon drift detector 100GV), and a Gatan966 Quantum ERS image filter (GIF) for EELS. We used an electron beam with an electron accelerating voltage of 200 kV and probe current of ~10 pA for the EELS analyses. The typical energy resolution of the EELS analyses was 0.2 to 0.3 eV, which was determined from the full-width half maximum of the measured zero-loss peak. The energy dispersion was set to 0.25 eV per channel for the analyses in the Fe L₃-edge region.

Supplementary Materials

This PDF file includes:

Figs. S1 to S11

Tables S1 and S2

References

REFERENCES AND NOTES

1. L. P. Keller, D. S. McKay, Discovery of vapor deposits in the lunar regolith. *Science* **261**, 1305–1307 (1993).
2. T. Noguchi, T. Nakamura, M. Kimura, M. E. Zolensky, M. Tanaka, H. Hashimoto, M. Konno, A. Nakato, T. Ogami, A. Fujimura, M. Abe, T. Yada, T. Mukai, M. Ueno, T. Okada, K. Shirai, Y. Ishibashi, R. Okazaki, Incipient space weathering observed on the surface of Itokawa dust particles. *Science* **333**, 1121–1125 (2011).
3. T. Noguchi, M. Kimura, T. Hashimoto, M. Konno, T. Nakamura, M. E. Zolensky, R. Okazaki, M. Tanaka, A. Tsuchiyama, A. Nakato, T. Ogami, H. Ishida, R. Sagae, S. Tsujimori, T. Matsumoto, J. Matsuno, A. Fujiwara, M. Abe, T. Yada, T. Mukai, M. Ueno, T. Okada, K. Shirai, Y. Ishibashi, Space weathered rims found on the surfaces of the Itokawa dust particles. *Meteorit. Planet. Sci.* **49**, 188–214 (2014).
4. S. K. Noble, L. P. Keller, C. M. Pieters, Evidence of space weathering in regolith breccias I: Lunar regolith breccias. *Meteorit. Planet. Sci.* **40**, 397–408 (2005).
5. S. K. Noble, L. P. Keller, C. M. Pieters, Evidence of space weathering in regolith breccias II: Asteroidal regolith breccias. *Meteorit. Planet. Sci.* **45**, 2007–2015 (2011).
6. C. M. Pieters, S. K. Noble, Space weathering on airless bodies. *J. Geophys. Res. Planets* **121**, 1865–1884 (2016).
7. K. D. Burgess, R. M. Stroud, Coordinated nanoscale compositional and oxidation state measurements of lunar space-weathered material. *J. Geophys. Res. Planets* **123**, 2022–2037 (2018).
8. B. Hapke, Space weathering from Mercury to the asteroid belt. *J. Geophys. Res.* **106**, 10039–10073 (2001).
9. S. K. Noble, C. M. Pieters, L. P. Keller, An experimental approach to understanding the optical effects of space weathering. *Icarus* **192**, 629–642 (2007).
10. E. Nakamura, A. Makishima, T. Moriguti, K. Kobayashi, R. Tanaka, T. Kunihiro, T. Tsujimori, C. Sekiguchi, H. Kitagawa, T. Ota, Y. Yachi, T. Yada, M. Abe, A. Fujimura, M. Ueno, T. Mukai, M. Yoshikawa, J. Kawaguchi, Space environment of an asteroid preserved on micrograins returned by the Hayabusa spacecraft. *Proc. Natl. Acad. Sci.* **109**, E624–E629 (2012).
11. F. Hörz, R. B. Schaaf, Asteroidal agglutinate formation and implications for asteroidal surfaces. *Icarus* **46**, 337–353 (1981).
12. S. Watanabe, M. Hirabayashi, N. Hirata, N. Hirata, R. Noguchi, Y. Shimaki, H. Ikeda, E. Tatsumi, M. Yoshikawa, S. Kikuchi, H. Yabuta, T. Nakamura, S. Tachibana, Y. Ishihara, T. Morota, K. Kitazato, N. Sakatani, K. Matsumoto, K. Wada, H. Senshu, R. Honda, S. Kameda, T. Fuse, H. Miyamoto, G. Komatsu, S. Sugita, T. Okada, N. Namiki, M. Arakawa, M. Ishiguro, M. Abe, R. Gaskell, E. Palmer, O. S. Barnouin, P. Michel, A. S. French, J. W. McMahon, D. J. Scheeres, P. A. Abell, Y. Yamamoto, S. Tanaka, K. Shirai, M. Matsuoka, M. Yamada, Y. Yokota, H. Suzuki, K. Yoshioka, Y. Cho, S. Tanaka, N. Nishikawa, T. Sugiyama, H. Kikuchi, R. Hemmi, T. Yamaguchi, N. Ogawa, G. Ono, Y. Mimasu, K. Yoshikawa, T. Takahashi, Y. Takei, A. Fujii, C. Hirose, T. Iwata, M. Hayakawa, S. Hosoda, O. Mori, H. Sawada, T. Shimada, S. Soldini, H. Yano, R. Tsukizaki, M. Ozaki, Y. Iijima, K. Ogawa, M. Fujimoto, T.-M. Ho, A. Moussi, R. Jaumann, J.-P. Bibring, C. Krause, F. Terui, T. Saiki, S. Nakazawa, Y. Tsuda, Hayabusa2 arrives at the carbonaceous asteroid 162173 Ryugu—A spinning top-shaped rubble pile. *Science* **364**, 268–272 (2019).
13. K. Kitazato, R. E. Milliken, T. Iwata, M. Abe, M. Ohtake, S. Matsuura, T. Arai, Y. Nakauchi, T. Nakamura, M. Matsuoka, H. Senshu, N. Hirata, T. Hiroi, C. Pilioret, R. Brunetto, F. Poulet, L. Riu, J.-P. Bibring, D. Takir, D. L. Domingue, F. Vilas, M. A. Barucci, D. Perna, E. Palomba, A. Galiano, K. Tsumura, T. Osawa, M. Komatsu, A. Nakato, T. Atai, N. Takato, T. Matsunaga, Y. Takagi, K. Matsumoto, T. Kouyama, Y. Yokota, E. Tatsumi, N. Sakatani, Y. Yamamoto, T. Okada, S. Sugita, R. Honda, T. Morota, S. Kameda, H. Sawada, C. Honda, M. Yamada, H. Suzuki, K. Yoshioka, M. Hayakawa, K. Ogawa, Y. Cho, K. Shirai, Y. Shimaki, N. Hirata, A. Yamaguchi, N. Ogawa, F. Terui, T. Yamaguchi, Y. Takei, T. Saiki, S. Nakazawa, S. Tanaka, M. Yoshikawa, S. Watanabe, Y. Tsuda, The surface composition of asteroid 162173 Ryugu from Hayabusa2 near-infrared spectroscopy. *Science* **364**, 272–275 (2019).
14. S. Sugita, R. Honda, T. Morota, S. Kameda, H. Sawada, E. Tatsumi, M. Yamada, C. Honda, Y. Yokota, T. Kouyama, N. Sakatani, K. Ogawa, H. Suzuki, T. Okada, N. Namiki, S. Tanaka, Y. Iijima, K. Yoshioka, M. Hayakawa, Y. Cho, M. Matsuoka, N. Hirata, N. Hirata, H. Miyamoto, D. Domingue, M. Hirabayashi, T. Nakamura, T. Hiroi, T. Michikami, P. Michel, R.-L. Ballouz, O. S. Barnouin, C. M. Ernest, S. E. Schröder, H. Kikuchi, R. Hemmi, G. Komatsu, T. Fukuhara, M. Taguchi, T. Arai, H. Seishu, H. Demura, Y. Ogawa, Y. Shimaki, T. Sekiguchi, T. G. Müller, A. Hagermann, T. Mizuno, H. Noda, K. Matsumoto, R. Yamada, Y. Ishihara, H. Ikeda, H. Araki, K. Yamamoto, S. Abe, F. Yoshida, A. Higuchi, S. Sasaki, S. Oshigami, S. Tsuruta, K. Asari, S. Tazawa, M. Shizugami, J. Kimura, T. Otsubo, H. Yabuta, S. Hasegawa, M. Ishiguro, S. Tachibana, E. Palmer, R. Gaskell, L. Le Corre, R. Jaumann, K. Otto, N. Schmitz, P. A. Abell, M. A. Barucci, M. E. Zolensky, F. Vilas, F. Thuillet, C. Sugimoto, N. Takaki, Y. Suzuki, H. Kamiyoshihara, M. Okada, K. Nagata, M. Fujimoto, M. Yoshikawa, Y. Yamamoto, K. Shirai, R. Noguchi, N. Ogawa, F. Terui, S. Kikuchi, T. Yamaguchi, Y. Oki, Y. Takano, H. Takeuchi, G. Ono, Y. Mimasu, K. Yoshikawa, T. Takahashi, Y. Takei, A. Fujii, C. Hirose, S. Nakazawa, S. Hosoda, O. Mori, T. Shimada, S. Soldini, T. Iwata, M. Abe, H. Yano, R. Tsukizaki, M. Ozaki, K. Hishiyama, T. Saiki, S. Watanabe, Y. Tsuda, The geomorphology, color, and thermal properties of Ryugu: Implications for parent-body processes. *Science* **364**, 252 (2019).

15. E. Tatsumi, C. Sugimoto, L. Riu, S. Sugita, T. Nakamura, T. Hiroi, T. Morota, M. Popescu, T. Michikami, K. Kitazato, M. Matsuoka, S. Kameda, R. Honda, M. Yamada, N. Sakatani, T. Kouyama, Y. Yokotata, C. Honda, H. Suzuki, Y. Cho, K. Ogawa, M. Hayakawa, H. Sawada, K. Yoshioka, C. Pilorget, M. Ishida, D. Domingue, N. Hirata, S. Sasaki, J. de Léon, M. A. Barucci, P. Michel, M. Suemitsu, T. Saiki, S. Tanaka, F. Terui, S. Nakazawa, S. Kikuchi, T. Yamaguchi, N. Ogawa, G. Ono, Y. Mimasu, K. Yoshikawa, T. Takahashi, Y. Takei, A. Fujii, Y. Yamamoto, T. Okada, C. Hirose, S. Hosoda, O. Mori, T. Shimada, S. Soldini, R. Tsukizaki, T. Mizuno, T. Iwata, H. Yano, M. Ozaki, M. Abe, M. Ohtake, N. Namiki, S. Tachibana, M. Arakawa, H. Ikeda, M. Ishiguro, K. Wada, H. Yabuta, H. Takeuchi, Y. Shimaki, K. Shirai, N. Hirata, Y. Iijima, Y. Tsuda, S. Watanabe, M. Yoshikawa, Collisional history of Ryugu's parent body from bright surface boulders. *Nat. Astron.* **5**, 39–45 (2021).
16. T. Yada, M. Abe, T. Okada, A. Nakato, K. Yogata, A. Miyazaki, K. Hatakeda, K. Kumagai, M. Nishimura, Y. Hitomi, H. Soejima, M. Yoshitake, A. Iwamae, S. Furuya, M. Uesugi, Y. Karouji, T. Usui, T. Hayashi, D. Yamamoto, R. Fukai, S. Sugita, Y. Cho, K. Yumoto, Y. Yabe, J.-P. Bibring, C. Pilorget, V. Hamm, R. Burunetto, L. Riu, L. Lourit, D. Loizeau, G. Lequertier, A. Moussi-Soffys, S. Tachibana, H. Sawada, R. Okazaki, Y. Takano, K. Sakamoto, Y. N. Miura, H. Yano, T. R. Ireland, T. Yamada, M. Fujimoto, K. Kitazato, N. Namiki, M. Arakawa, N. Hirata, H. Yurimoto, T. Nakamura, T. Noguchi, H. Yabuta, H. Naraoka, M. Ito, E. Nakamura, K. Uesugi, K. Kobayashi, T. Michikami, H. Kikuchi, N. Hirata, Y. Ishihara, K. Matsumoto, H. Noda, R. Noguchi, Y. Shimaki, K. Shirai, K. Ogawa, K. Wada, H. Snshu, Y. Yamamoto, T. Morota, R. Honda, C. Honda, Y. Yokota, M. Matsuoka, N. Sakatani, E. Tatsumi, A. Miura, M. Yamada, A. Fujii, C. Hirose, S. Hosoda, H. Ikeda, T. Iwata, S. Kikuchi, Y. Mimasu, O. Mori, N. Ogawa, G. Ono, T. Shimada, S. Soldini, T. Takahashi, Y. Takei, H. Takeuchi, R. Tsukizaki, K. Yoshikawa, F. Terui, S. Nakazawa, S. Tanaka, T. Saiki, M. Yoshikawa, S. Watanabe, Y. Tsuda, Preliminary analysis of the Hayabusa2 samples returned from C-type asteroid Ryugu. *Nat. Astron.* **6**, 214–220 (2022).
17. S. Tachibana, H. Sawada, R. Okazaki, Y. Takano, K. Sakamoto, Y. N. Miura, C. Okamoto, H. Yano, S. Yamanouchi, P. Michel, Y. Zhang, S. Schwartz, F. Thuillet, H. Yurimoto, T. Nakamura, T. Noguchi, H. Yabuta, H. Naraoka, A. Tsuchiyama, N. Imae, K. Kurosawa, A. M. Nakamura, K. Ogawa, S. Sugita, T. Morota, R. Honda, S. Kameda, E. Tatsumi, Y. Cho, K. Yoshioka, Y. Yokota, M. Hayakawa, M. Matsuoka, N. Sakatani, M. Yamada, T. Kouyama, H. Suzuki, C. Honda, T. Yoshimitsu, T. Kubota, H. Demura, T. Yada, M. Nishimura, K. Yogata, A. Nakato, M. Yoshitake, A. I. Suzuki, S. Furuya, K. Hatakeda, A. Miyazaki, K. Kumagai, T. Okada, M. Abe, T. Usui, T. R. Ireland, M. Fujimoto, T. Yamada, M. Arakawa, H. C. Connolly Jr., A. Fujii, S. Hasegawa, N. Hirata, N. Hirata, C. Hirose, S. Hosoda, Y. Iijima, H. Ikeda, M. Ishiguro, Y. Ishihara, T. Iwata, S. Kikuchi, K. Kitazato, D. S. Lauretta, G. Libourel, B. Marty, K. Matsumoto, T. Michikami, Y. Mimasu, A. Miura, O. Mori, K. Nakamura-Messenger, N. Namiki, A. N. Nguyen, L. R. Nittler, H. Noda, R. Noguchi, N. Ogawa, G. Ono, M. Ozaki, H. Senshu, T. Shimada, Y. Shimaki, K. Shirai, S. Soldini, T. Takahashi, Y. Takei, H. Takeuchi, R. Tsukizaki, K. Wada, Y. Yamamoto, K. Yoshikawa, K. Yumoto, M. E. Zolensky, S. Nakazawa, F. Terui, S. Tanaka, T. Saiki, M. Yoshikawa, S. Watanabe, Y. Tsuda, Pebbles and sand on asteroid (162173): In situ observation and particles returned to Earth. *Science* **375**, 1011–1016 (2022).
18. T. Yokoyama, K. Nagashima, I. Nakai, E. D. Young, Y. Abe, J. Aléon, C. M. O. Alexander, S. Amari, Y. Amelin, K. Bajo, M. Bizzarro, A. Bouvier, R. W. Carlson, M. Chaussidon, B.-G. Choi, N. Dauphas, A. M. Davis, T. D. Rocco, W. Fujiya, R. Fukai, I. Gautam, M. K. Haba, Y. Hibiya, H. Hidaka, H. Homma, P. Hoppe, G. R. Huss, K. Ichida, T. Iizuka, T. R. Ireland, A. Ishikawa, M. Ito, S. Itho, N. Kawasaki, N. T. Kita, K. Kitajima, T. Kleine, S. Komatani, A. N. Krot, M. Liu, Y. Masuda, K. D. McKeegan, M. Morita, K. Motomura, F. Moynier, A. Nguyen, L. Nittler, M. Onose, A. Pack, C. Park, L. Piani, L. Qin, S. S. Russell, N. Sakamoto, M. Schönbachler, L. Tafla, H. Tang, K. Terada, Y. Terada, T. Usui, S. Iwada, M. Wadhwa, R. J. Walker, K. Yamashita, Q. Yin, S. Yoneda, H. Yui, A. Zhang, H. C. Connolly Jr., D. S. Lauretta, T. Nakamura, H. Naraoka, T. Noguchi, R. Okazaki, K. Sakamoto, H. Yabuta, M. Abe, M. Awakawa, A. Fujii, M. Hayakawa, N. Hirata, K. Kawahara, S. Kikuchi, K. Kitazato, K. Matsumoto, M. Matsuoka, T. Michikami, Y. Mimasu, A. Miura, T. Morota, S. Nakazawa, N. Namiki, H. Noda, R. Noguchi, N. Ogawa, K. Ogawa, T. Okada, C. Okamoto, G. Ono, M. Ozaki, T. Saiki, N. Sakatani, H. Sawada, H. Senshu, Y. Shimaki, K. Shirai, S. Sugita, Y. Takei, H. Takeuchi, Y. Yamamoto, H. Yano, Y. Yokota, K. Yoshihara, M. Yoshikawa, K. Yoshikawa, S. Furuya, K. Hatakeda, T. Hayashi, Y. Hitomi, K. Kumagai, A. Miyazaki, A. Nakato, M. Nishimura, H. Soejima, A. Suzuki, T. Yada, D. Yamamoto, K. Yogata, M. Yoshitake, S. Tachibana, H. Yurimoto, Samples returned from the asteroid Ryugu are similar to Ivuna-type carbonaceous meteorites. *Science* **379**, eabn7850 (2023).
19. T. Nakamura, M. Matsumoto, K. Amano, Y. Enokido, M. E. Zolensky, T. Mikouchi, H. Genda, S. Tanaka, M. Y. Zolotov, K. Kurosawa, S. Wakita, R. Hyodo, H. Nagano, D. Nakashima, Y. Takahashi, Y. Fujioka, M. Kikuri, E. Kagawa, M. Matsuoka, A. J. Breareley, A. Tsuchiyama, M. Uesugi, J. Matsuno, Y. Kimura, M. Sato, R. E. Milliken, E. Tatsumi, S. Sugita, T. Hiroi, K. Kitazato, D. Brownlee, D. J. Joswiak, M. Takahashi, K. Ninomiya, T. Takahashi, T. Osawa, K. Terada, F. E. Brenker, B. J. Tkalcic, L. Vincze, R. Brunetto, A. A. Toppani, Q. H. Chan, M. Roskoz, J.-C. Viennet, P. Beck, E. E. Alp, T. Michikami, Y. Nagaashi, T. Tsuji, Y. Ino, J. Martinez, J. Han, A. Dolocan, R. J. Bodnar, M. Tanaka, H. Yoshida, K. Sugiyama, A. J. King, K. Fukushi, H. Suga, S. Yamashita, T. Kawai, K. Inoue, A. Nakato, T. Noguchi, F. Vilas, A. R. Hendrix, C. Jaramillo-Correa, D. L. Domingue, Z. Gainsforth, C. Engrand, J. Duprat, S. S. Russell, E. Bonato, C. Ma, T. Kawamoto, T. Wada, S. Watanabe, R. Endo, S. Enju, L. Riu, S. Rubino, P. Tack, S. Takeshita, Y. Takeuchi, A. Takeuchi, A. Takigawa, D. Takir, T. Tanigaki, A. Taniguchi, K. Tsukamoto, T. Yagi, S. Yamada, K. Yamamoto, Y. Yamashita, M. Yasutake, K. Uesugi, I. Umegaki, I. Chiu, T. Ishizaki, S. Okumura, E. Palomba, C. Pilorget, S. M. Potin, A. Alasli, S. Anada, Y. Araki, N. Sakatani, C. Schultz, O. Sekizawa, S. D. Sitzman, K. Sugijara, M. Sun, E. Dartois, E. De Pauw, Z. Dionnet, Z. Djouadi, G. Falkenberg, R. Fujita, T. Fukuma, I. R. Gearba, K. Gagiya, M. Y. Hu, T. Kato, T. Kawamura, M. Kimura, M. K. Kubo, F. Langenhorst, C. Lantz, B. Lavina, M. Lindner, J. Zhao, B. Vekemans, D. Baklouti, B. Bazi, F. Borondics, S. Nagsawa, G. Nishiyama, K. Nitta, J. Mathurin, T. Matsumoto, I. Mitsukawa, H. Miura, A. Miyake, Y. Miyake, H. Yurimoto, R. Okazaki, H. Yabuta, H. Maraoka, K. Sakamoto, S. Tachibana, H. C. Connolly Jr., D. S. Lauretta, M. Yoshitake, M. Yoshikawa, K. Yoshihara, Y. Yokota, K. Yogata, H. Yano, Y. Yamamoto, D. Yamamoto, M. Yamama, T. Yamada, T. Yada, K. Wada, T. Usui, R. Tsukizaki, F. Terui, H. Takeuchi, Y. Takei, A. Iwamae, H. Soejima, K. Shirai, Y. Shimaki, H. Senshu, H. Sawada, T. Saiki, M. Ozaki, G. Ono, T. Okda, N. Ogawa, K. Ogawa, R. Noguchi, H. Noda, M. Nishimura, N. Namiki, S. Nakazawa, T. Morota, A. Miyazaki, A. Miura, Y. Mimasu, K. Matsumoto, K. Kumagai, T. Kouyama, S. Kikuchi, K. Kawahara, S. Kameda, T. Iwata, Y. Ishihara, M. Ishiguro, H. Ikeda, S. Hosoda, R. Honda, C. Honda, Y. Hitomi, N. Hirata, N. Hirata, T. Hayashi, M. Hayakawa, K. Hatakeda, S. Furuya, R. Fukai, A. Fujii, Y. Cho, M. Arakawa, M. Abe, S. Watanabe, Y. Tsuda, Formation and evolution of carbonaceous asteroid Ryugu: Direct evidence from returned samples. *Science* **379**, eabn8671 (2023).
20. T. Noguchi, T. Matsumoto, A. Miyake, Y. Igami, M. Haruta, H. Saito, S. Hata, Y. Seto, M. Miyahara, N. Tomioka, H. A. Ishii, J. P. Bradley, K. K. Ohtaki, E. Dobrica, H. Leroux, C. Le Guillou, D. Jacob, F. de la Pena, S. Laforet, M. Marinova, F. Langenhorst, D. Harries, P. Beck, T. H. V. Phan, R. Rebois, N. M. Abreu, J. Gray, T. Zaga, P.-M. Zanetta, M. S. Thompson, R. Stroud, K. Burgess, B. A. Cymes, J. C. Brigidges, M. R. Lee, L. Daly, P. A. Bland, M. E. Zolensky, D. R. Frank, J. Martinez, A. Tsuchiyama, M. Yasutake, J. Matsuno, S. Okumura, I. Mitsukawa, K. Uesugi, A. Takeuchi, M. Sun, S. Enju, A. Takigawa, T. Michikami, T. Nakamura, M. Matsumoto, Y. Nakachi, M. Abe, M. Arakawa, A. Fujii, M. Hayakawa, N. Hirata, N. Hirata, R. Honda, C. Honda, S. Hosoda, Y. I. Iijima, H. Ikeda, M. Ishiguro, Y. Ishihara, T. Iwata, K. Kawahara, S. Kikuchi, K. Kitazato, K. Matsumoto, M. Matsuoka, Y. Mimasu, A. Miura, T. Morota, N. Satoru, N. Namiki, H. Noda, R. Noguchi, N. Ogawa, K. Ogawa, T. Okada, C. Okamoto, G. Ono, M. Ozaki, T. Saiki, N. Sakatani, H. Sawada, H. Senshu, Y. Shimaki, K. Shirai, S. Sugita, Y. Takei, H. Takeuchi, S. Tanaka, E. Tatsumi, F. Terui, R. Tsukizaki, K. Wada, M. Yamada, T. Yamada, Y. Yamamoto, H. Yano, Y. Yokota, K. Yoshihara, M. Yoshikawa, K. Yoshikawa, R. Fukai, S. Furuya, K. Hatakeda, T. Hayashi, Y. Hitomi, K. Kumagai, A. Miyazaki, A. Nakato, M. Nishimura, H. Soejima, A. I. Suzuki, T. Usui, T. Yada, D. Yamamoto, K. Yogata, M. Yoshitake, H. C. Connolly Jr., D. S. Lauretta, H. Yurimoto, K. Nagashima, N. Kawasaki, N. Sakamoto, R. Okazaki, H. Yabuta, H. Naraoka, K. Sakamoto, S. Tachibana, S. Watanabe, Y. Tsuda, A dehydrated space-weathered skin cloaking the hydrated interior of Ryugu. *Nat. Astron.* (2022).
21. M. Ito, N. Tomioka, M. Uesugi, A. Yamaguchi, N. Shirai, T. Ohigashi, M. Liu, R. C. Greenwood, M. Kimura, N. Imae, K. Uesugi, A. Nakato, K. Yogata, H. Yuzawa, Y. Kodama, A. Tsuchiyama, M. Yasutake, R. Findlay, L. A. Franchi, J. A. Malley, K. A. McCain, N. Matsuda, K. D. McKeegan, K. Hirahara, A. Takeuchi, S. Skimot, I. Sakurai, I. Okada, Y. Karouji, M. Arakawa, A. Fujii, M. Fujimoto, M. Hayakawa, N. Hirata, N. Hirata, R. Honda, C. Honda, S. Hosoda, Y. Iijima, H. Ikeda, M. Ishiguro, Y. Ishihara, T. Iwata, K. Kawahara, S. Kikuchi, K. Kitazato, K. Matsumoto, M. Matsuoka, T. Michikami, Y. Mimasu, A. Miura, O. Mori, T. Morota, S. Nakazawa, N. Namiki, H. Noda, R. Noguchi, N. Ogawa, K. Ogawa, T. Okada, C. Okamoto, G. Ono, M. Ozaki, T. Saiki, T. Sakatani, E. Tatsumi, F. Terui, R. Tsukizaki, K. Wada, M. Yamada, T. Yamada, Y. Yamamoto, H. Yano, Y. Yokota, K. Yoshihara, M. Yoshikawa, K. Yoshikawa, R. Fukai, S. Furuya, K. Hatakeda, T. Haysashi, Y. Hitomi, K. Kumagai, A. Miyazaki, M. Nishimura, H. Soejima, A. Iwamae, D. Yamamoto, M. Yoshitake, T. Yoda, M. Abe, T. Usui, S. Watanabe, Y. Tsuda, A pristine record of outer Solar System materials from asteroid Ryugu's returned sample. *Nat. Astron.* **6**, 1163–1171 (2022).
22. E. Nakamura, K. Kobayashi, R. Tanaka, T. Kunihiro, H. Kitagawa, C. Potisil, T. Ota, C. Sakaguchi, M. Yamanaka, D. M. Ratnayake, H. Tripathi, R. Kumar, M. Avramescu, H. Tsuchida, Y. Yachi, H. Miura, M. Abe, R. Fukai, S. Furuya, K. Hatakeda, T. Hayashi, M. Nishimura, T. Okada, H. Soejima, S. Sugita, A. Suzuki, T. Usui, T. Yada, D. Yamamoto, K. Yogata, M. Yoshitake, M. Arakawa, A. Fujii, M. Hayakawa, N. Hirata, N. Hirata, R. Honda, C. Honda, S. Hosoda, Y. Iijima, H. Ikeda, M. Ishiguro, Y. Ishihara, T. Iwata, K. Kawahara, S. Kikuchi, K. Kitazato, K. Matsumoto, M. Matsuoka, T. Michikami, Y. Mimasu, A. Miura, T. Morota, S. Nakazawa, N. Namiki, H. Noda, R. Noguchi, N. Ogawa, K. Ogawa, C. Okamoto, G. Ono, M. Ozaki, T. Saiki, N. Sakatani, H. Takeuchi, S. Tanaka, E. Tatsumi, F. Terui, R. Tsukizaki, K. Wada, M. Yamada, T. Yamada, Y. Yamamoto, H. Yano, Y. Yokota, K. Yoshihara, M. Yoshikawa, K. Yoshikawa, M. Fujimoto, S. Watanabe, Y. Tsuda, On the origin and evolution of the asteroid Ryugu: A comprehensive geochemical perspective. *Proc. Jpn. Acad. Ser. B Phys. Biol. Sci.* **98**, 227–282 (2022).
23. T. Matsumoto, D. Harries, F. Langenhorst, A. Miyake, T. Noguchi, Iron whiskers on asteroid Itokawa indicate sulfide destruction by space weathering. *Nat. Commun.* **11**, 1117 (2020).

24. T. Matsumoto, T. Noguchi, A. Miyake, Y. Igami, M. Haruta, Y. Seto, M. Miyahara, N. Tomioka, H. Saito, S. Hata, D. Harries, A. Takigawa, Y. Nakauchi, S. Tachibana, T. Nakamura, M. Matsumoto, H. A. Ishii, J. P. Bradley, K. Ohtaki, E. Dobrică, H. Leroux, C. L. Guillou, D. Jacob, F. de la Peña, S. Laforet, M. Marinova, F. Langenhorst, P. Beck, T. H. V. Phan, R. Rebois, N. M. Abreu, J. Gray, T. Zega, P.-M. Zanetta, M. S. Thompson, R. Stroud, K. Burgess, B. A. Cymes, J. C. Bridges, L. Hicks, M. R. Lee, L. Daly, P. A. Bland, M. E. Zolensky, D. R. Frank, J. Martinez, A. Tsuchiyama, M. Yasutake, J. Matsuno, S. Okumura, I. Mitsukawa, K. Uesugi, M. Uesugi, A. Takeuchi, M. Sun, S. Enju, T. Michikami, H. Yurimoto, R. Okazaki, H. Yabuta, H. Naraoka, K. Sakamoto, T. Yada, M. Nishimura, A. Nakato, A. Miyazaki, K. Yogata, M. Abe, T. Okada, T. Usui, M. Yoshikawa, T. Saiki, S. Tanaka, F. Terui, S. Nakazawa, S.-I. Watanabe, Y. Tsuda, Influx of nitrogen-rich material from the outer Solar System indicated by iron nitride in Ryugu samples. *Nat. Astron.* (2023).
25. K. Lodders, Relative atomic solar system abundances, mass fractions, and atomic masses of the elements and their isotopes, composition of the solar photosphere, and compositions of the major chondritic meteorite groups. *Space Sci. Rev.* **217**, 44 (2021).
26. K. Tomeoka, P. R. Buseck, Matrix mineralogy of the Orgueil CI carbonaceous chondrite. *Geochim. Cosmochim. Acta* **52**, 1627–1640 (1988).
27. J. Alfing, M. Patzek, A. Bischoff, Modal abundances of coarse-grained (>5 µm) components within CI-chondrites and their individual clasts—Mixing of various lithologies on the CI parent body(ies). *Geochem.* **79**, 125532 (2019).
28. P. R. Buseck, H. Bo-Jun, Conversion of carbonaceous material to graphite during metamorphism. *Geochim. Cosmochim. Acta* **49**, 2003–2016 (1985).
29. R. Matassa, S. Orlanducci, E. Tamburri, V. Guglielmotti, D. Sordi, M. L. Terranova, D. Passeri, M. Rossi, Characterization of carbon structures produced by graphene self-assembly. *J. Appl. Cryst.* **47**, 222–227 (2014).
30. T. B. Shiell, D. G. McCulloch, J. E. Bradby, B. Haberl, Nanocrystalline hexagonal diamond formed from glassy carbon. *Sci. Rep.* **6**, 37232 (2016).
31. H. Campins, J. León, A. Morbidelli, J. Licandro, J. Gayon-Markt, M. Delbó, P. Michel, The origin of asteroid 162173 (1999 JU₃). *Astron. J.* **146**, 26 (2013).
32. K. J. Walsh, M. Delbó, W. F. Bottke, D. Vokrouhlický, D. S. Lauretta, Introducing the eulalia and new Polana asteroid families: Re-assessing primitive asteroid families in the inner Main Belt. *Icarus* **225**, 283–297 (2013).
33. T. Morota, S. Sugita, Y. Sho, M. Kanamaru, E. Tatsumi, N. Sakatani, R. Honda, N. Hirata, H. Kikuchi, M. Yamada, Y. Yokota, S. Kameda, M. Matsuoka, H. Sawada, C. Honda, T. Kouyama, K. Ogawa, H. Suzuki, K. Yoshioka, M. Hayakawa, N. Hirata, M. Hirabayashi, H. Miyamoto, T. Michikami, T. Hiroi, R. Hemmi, O. S. Barnouin, C. M. Ernst, K. Kitazato, T. Nakamura, L. Riu, H. Sehshu, H. Kobayashi, S. Sasaki, G. Komatsu, N. Tanabe, Y. Fujii, T. Irie, M. Suemitsu, N. Takaki, C. Sugimoto, K. Yumoto, M. Ishida, H. Kato, K. Moroi, D. Domingue, P. Michel, C. Pilorget, T. Iwata, M. Abe, M. Ohtake, Y. Nakauchi, K. Tsumura, H. Yabuta, Y. Ishihara, R. Noguchi, K. Matsumoto, A. Miura, N. Namiki, S. Tachibana, M. Arakawa, H. Ikeda, K. Wada, T. Mizuno, C. Hirose, S. Hosoda, O. Mori, T. Shimada, S. Soldini, R. Tsukizaki, H. Yano, M. Ozaki, H. Takeuchi, Y. Yamamoto, T. Okada, Y. Shimaki, K. Shirai, Y. Iijima, H. Noda, S. Kikuchi, T. Yamaguchi, N. Ogawa, G. Ono, Y. Mimasu, K. Yoshikawa, T. Takahashi, Y. Takei, A. Fujii, S. Nakazawa, F. Terui, S. Tanaka, M. Yoshikawa, T. Saiki, S. Watanabe, Y. Tsuda, Sample collection from asteroid (162173) Ryugu by Hayabusa2: Implications for surface evolution. *Science* **368**, 654–659 (2020).
34. R. Okazaki, Y. Miura, Y. Takano, H. Sawada, K. Sakamoto, T. Yada, K. Yamada, S. Kawaguchi, Y. Matsui, K. Hashizume, A. Ishida, M. W. Bradley, B. Marty, D. Byrne, E. Furi, A. Meshik, O. Pradivseva, H. Busemann, M. E. I. Riebe, J. Gilmour, J. Park, K. Bajo, K. Righter, S. Sakai, S. Sekimoto, F. Kitajima, S. A. Crowther, N. Iwata, N. Shirai, M. Ebihara, R. Yokochi, K. Nishizumi, K. Nagao, J. I. Lee, P. Clay, A. Kano, M. W. Caffee, R. Uemura, M. Inagaki, D. Krietsch, C. Maden, M. Yamamoto, L. Fawcett, T. Lawton, T. Nakamura, H. Naraoka, T. Noguchi, H. Yabuta, H. Yurimoto, Y. Tsuda, S. Watanabe, M. Abe, M. Arakawa, A. Fujii, M. Hayakawa, N. Hirata, N. Hirata, R. Honda, C. Honda, S. Hosoda, Y. Iijima, H. Ikeda, M. Ishiguro, Y. Ishihara, T. Iwata, K. Kawahara, S. Kikuchi, K. Kitazato, K. Matsumoto, M. Matsuoka, T. Michikami, Y. Mimasu, A. Miura, T. Morota, S. Nakazawa, N. Namiki, H. Noda, R. Noguchi, N. Ogawa, K. Ogawa, T. Okada, C. Okamoto, G. Ono, M. Ozaki, T. Saiki, N. Sakatani, H. Senshu, Y. Shimaki, K. Shirai, S. Sugita, Y. Takei, H. Takeuchi, S. Tanaka, E. Tatsumi, F. Terui, R. Tsukizaki, K. Wada, M. Yamada, T. Yamada, Y. Yamamoto, H. Yano, Y. Yokota, K. Yoshihara, M. Yoshikawa, K. Yoshikawa, S. Furuya, K. Hotakada, T. Hayashi, Y. Hitomi, K. Kumagai, A. Miyazaki, A. Nakato, M. Nishimura, H. Soejima, A. Iwamae, D. Yamamoto, K. Yogata, M. Yoshitake, R. Fukai, T. Usui, T. Ireland, H. C. Connolly Jr., D. Lauretta, S. Tachibana, First asteroid gas sample delivered by the Hayabusa2 mission: A treasure box from Ryugu. *Sci. Adv.* **8**, eabo7239 (2022).
35. P. Pokorný, D. Janches, M. Sarantos, J. R. Szalay, M. Horányi, D. Nesvorný, M. J. Kuchner, Meteoroids at the moon: Orbital properties, surface vaporization, and impact ejecta production. *J. Geophys. Res. Planets* **124**, 752–778 (2019).
36. M. Zolensky, T. Mikouchi, K. Hagiya, K. Ohsumi, M. Komatsu, A. Cheng, L. Le, Evidence for impact shock and regolith transportation on CM, CI, and CV chondrite parent asteroids. *Meteorit. Planet. Sci.* **57**, 1902–1919 (2022).
37. G. Kullerød, R. A. Yund, G. H. Mou, Phase relations in the Cu-Fe-S, Cu-Ni-S, and Fe-Ni-S systems, in *Magmatic Ore Deposits*, H. D. B. Wilson Ed. (Economic Geology Monograph, 1969), vol. 4, 323–343.
38. A. Kitakaze, T. Machida, R. Komatsu, Phase relations in the Fe-Ni-S system from 875 to 650°C. *Can. Mineral.* **54**, 1175–1186 (2016).
39. H. Leroux, F. J. M. Rietmeijer, M. A. Velbel, A. J. Brearley, D. Jacob, F. Langenhorst, J. Bridges, T. J. Zega, R. M. Stroud, P. Cordier, R. P. Harvey, M. Lee, M. Gounelle, M. E. Zolensky, A TEM study of thermally modified comet 81P/Wild 2 dust particles by interactions with the aerogel matrix during the Stardust capture process. *Meteorit. Planet. Sci.* **43**, 97–120 (2008).
40. M. Zolensky, R. Barrett, L. Browning, Mineralogy and composition of matrix and chondrule rims in carbonaceous chondrites. *Geochim. Cosmochim. Acta* **57**, 3123–3148 (1993).
41. L. S. Schramm, D. E. Brownlee, M. M. Wheelock, Major element composition of stratospheric micrometeorites. *Meteoritics* **24**, 99–112 (1989).
42. G. Kurat, C. Koeberl, T. Presper, F. Brandstätter, M. Maurette, Petrology and geochemistry of Antarctic micrometeorites. *Geochim. Cosmochim. Acta* **58**, 3879–3904 (1994).
43. M. Gounelle, C. Engrand, M. Maurette, G. Kurat, K. D. McKeegan, F. Brandstätter, Small Antarctic micrometeorites: A mineralogical and in situ oxygen isotope study. *Meteorit. Planet. Sci.* **40**, 917–932 (2005).
44. L. P. Keller, S. Messenger, On the origins of GEMS grains. *Geochim. Cosmochim. Acta* **75**, 5336–5365 (2011).
45. J. P. Bradley, Early solar nebula grain—Interplanetary dust particles., in *Treatise on Geochemistry (Second Edition)*, A. M. Davis, Ed. (Elsevier, 2014), pp. 287–308.
46. G. Matrajt, S. Messenger, D. Brownlee, D. Joswiak, Diverse forms of primordial organic matter identified in interplanetary dust particles. *Meteorit. Planet. Sci.* **47**, 525–549 (2012).
47. K. Awazu, Ablation and compaction of amorphous SiO₂ irradiated with ArF excimer laser. *J. Non Cryst. Solids* **337**, 241–253 (2004).
48. M. J. Loeffler, C. A. Dukes, R. Christoffersen, R. A. Baragiola, Space weathering of silicates simulated by successive laser irradiation: In situ reflectance measurements of Fe₉₀, Fe₉₉₊, and SiO₂. *Meteorit. Planet. Sci.* **51**, 167–180 (2016).
49. J. Akai, T-T diagram of serpentine and saponite, and estimation of metamorphic heating degree of Antarctic carbonaceous chondrites. *Natl. Inst. Polar Res.* **5**, 120–135 (1992).
50. Y. Fei, C. M. Bertka, L. W. Finger, High-pressure iron-sulfur compound, Fe₃S₂, and melting relations in the Fe-FeS system. *Science* **275**, 1621–1623 (1997).
51. V. Raghavan, Fe-Ni-S (iron-nickel-sulfur). *J. Phase Equilibria Diffus.* **25**, 373–381 (2004).
52. A. T. Kearsley, M. J. Burchell, F. Hörtz, M. J. Cole, C. S. Schwandt, Laboratory simulation of impacts on aluminum foils of the Stardust spacecraft: Calibration of dust particle size from comet Wild-2. *Meteorit. Planet. Sci.* **41**, 167–180 (2006).
53. M. C. Price, A. T. Kearsley, M. J. Burchell, F. Hörtz, J. Borg, J. C. Bridges, M. J. Cole, C. Floss, G. Graham, S. F. Green, P. Hoppe, H. Leroux, K. K. Marhas, N. Park, R. Stroud, F. J. Stadermann, N. Telisch, P. J. Wozniakiewicz, Comet 81P/Wild 2: The size distribution of finer (sub-10 µm) dust collected by the Stardust spacecraft. *Meteorit. Planet. Sci.* **45**, 1409–1428 (2010).
54. A. Shu, S. Bugiel, E. Grün, J. Hillier, M. Horányi, T. Munsat, R. Srama, Cratering studies in polyvinylidene fluoride (PVDF) thin films. *Planet. Space Sci.* **89**, 29–35 (2013).
55. D. Nesvorný, P. Jenniskens, H. Levison, W. F. Bottke, D. Vokrouhlický, M. Gounelle, Cometary origin of the zodiacal cloud and carbonaceous micrometeorites. Implications for hot debris disks. *Astrophys. J.* **713**, 816–836 (2010).
56. D. Nesvorný, D. Janches, D. Vokrouhlický, P. Rokorný, W. Bottke, P. Jenniskens, Dynamical model for the zodiacal cloud and sporadic meteors. *Astrophys. J.* **743**, 129 (2011).
57. A. T. Kearsley, J. Borg, G. A. Graham, M. J. Burchell, M. J. Cole, H. Leroux, J. C. Bridges, F. Hörtz, P. J. Wozniakiewicz, P. A. Bland, J. P. Bradley, Z. R. Dai, N. Teslich, T. See, P. Hoppe, P. R. Heck, J. Huth, F. J. Stadermann, C. Floss, K. Marhas, T. Stephan, J. Leitner, Dust from comet Wild 2: Interpreting particle size, shape, structure, and composition from impact features on the Stardust aluminum foils. *Meteorit. Planet. Sci.* **43**, 41–73 (2008).
58. P. Wu, G. Eriksson, A. D. Pelton, M. Blander, Prediction of the thermodynamic properties and phase diagrams of silicate systems—Evaluation of the FeO-MgO-SiO₂ system. *ISIJ Int.* **33**, 26–35 (1993).
59. A. B. Thompson, M. Aerts, A. C. Hack, Liquid immiscibility in silicate melts and related systems. *Rev. Mineral. Geochem.* **65**, 99–127 (2007).
60. C. Jäger, F. J. Molster, J. Dorschner, T. Henning, H. Mutschke, L. B. F. M. Waters, Steps toward interstellar silicate mineralogy IV the crystalline revolution. *Astron Astrophys.* **339**, 904–916 (1998).
61. M. S. Thompson, R. Christoffersen, T. J. Zega, L. P. Keller, Microchemical and structural evidence for space weathering in soils from asteroid Itokawa. *Earth Planets Space* **66**, 89 (2014).
62. A. Miyake, J. Matsuno, S. Toh, Sample preparation toward seamless 3D imaging technique from micrometer to nanometer scale. *Microscopy(Oxf)* **63**, i24–i25 (2014).
63. M. Matsumoto, A. Tsuchiyama, A. Nakato, J. Matsuno, A. Miyake, A. Kataoka, M. Ito, N. Tomioka, Y. Kodama, K. Uesugi, A. Takeuchi, T. Nakano, E. Vaccaro, Discovery of fossil asteroidal ice in primitive meteorite Acfer 094. *Sci. Adv.* **5**, eaax5078 (2019).
64. A. Tsuchiyama, T. Nakano, K. Uesugi, M. Uesugi, A. Takeuchi, Y. Suzuki, R. Noguchi, T. Matsumoto, J. Matsuno, T. Nagano, Y. Imai, T. Nakamura, T. Ogami, T. Noguchi, M. Abe, T. Yada, A. Fujimura, Analytical dual-energy microtomography: A new method for

- obtaining three-dimensional mineral phase images and its application to Hayabusa samples. *Geochim. Cosmochim. Acta* **116**, 5–16 (2013).
65. A. Takeuchi, K. Uesugi, Y. Suzuki, Three-dimensional phase-contrast x-ray microtomography with scanning-imaging x-ray microscope optics. *J. Synchrotron Radiat.* **20**, 793–800 (2013).
 66. M. Matsumoto, A. Tsuchiyama, A. Miyake, M. Ito, J. Matsuno, K. Uesugi, A. Takeuchi, Y. Kodama, M. Yasutake, E. Vaccaro, Three-dimensional microstructure and mineralogy of a cosmic symplectite in the Acfer 094 carbonaceous chondrite: Implication for its origin. *Geochim. Cosmochim. Acta* **323**, 220–241 (2022).
 67. M. Watanabe, D. B. Williams, The quantitative analysis of thin specimens: A review of progress from the Cliff-Lorimer to the new ζ -factor methods. *J. Microsc.* **221**, 89–109 (2006).
 68. P. Waldner, A. D. Pelton, Thermodynamic modeling of the Fe-S system. *J. Phase Equilibria Diffus.* **26**, 23–38 (2005).
 69. R. Y. Lin, D. C. Hu, Y. A. Chang, Thermodynamics and phase relationships of transition metal-sulfur system: II. The nickel-sulfur system. *Metall. Mater. Trans. B* **9**, 531–538 (1978).

Acknowledgments: We thank T. Miyazaki for helping TEM observation; T. Konno, Y. Kodama, and K. Takenaka for helping FIB sample preparation; and T. Matsumoto for helping SEM observation. We also thank anonymous reviewers for constructive comments. The XnCT experiments at SPring-8 were conducted under the proposal numbers 2021B1600, 2021B0188,

and 2022A0188. **Funding:** This work was supported by JSPS KAKENHI grant number 19 K14776 for M.M., JSPS KAKENHI grant number 20H00205 for A.Tsuchiyama, and M.M., JSPS KAKENHI grant number 20H05846 for S.Tac. and M.M., and the NASA Hayabusa2 Participating Scientist Program for M.Z. **Author contributions:** Supervision: M.M., H.N., S.W., S.Tac., and Y.T. Project administration: S.N., S.-i.W., H.N., S.Tac., T.U., Y.T., K.S., F.T., M.M., S.Tan., M.Yo., and H.Ya. Resources: T.Y., M.N., A.N., A.Miyaz., K.Y., M.A., T.O., T.S., S.N., M.Ya., and A.Miyake. Conceptualization: M.M., T.Na., M.Z., J.M., K.U., Y.T., H.Yu., and Y.E. Methodology: M.M., M.Ya., K.U., A.Miyak., J.M., T.Y., Y.T., and A.Ts. Investigation: M.M., T.Na., J.M., A.Ts., A.N., M.K., S.E., S.O., I.M., M.S., M.H., Y.I., M.Ya., M.Z., S.N., S.-i.W., A.Ta., K.U., F.T., T.S., and A.Miyak. Formal analysis: M.M., M.Ya., J.M., and M.S. Visualization: J.M., M.M., and M.Z. Data curation: M.M. and M.Ya. Software: M.Ya., A.Ta., J.M., and K.U. Validation: M.M., M.Ya., I.M., J.M., K.U., H.Yu., and A.Ts. Writing—original draft: M.M. Writing—review and editing: A.Ts., T.No., K.U., T.O., H.Yu., and R.O. Funding acquisition: S.Tac., M.M., and A.Ts. **Competing interests:** The authors declare that they have no competing interests. **Data and materials availability:** All data needed to evaluate the conclusions in the paper are present in the paper and/or the Supplementary Materials.

Submitted 14 May 2023
Accepted 21 December 2023
Published 19 January 2024
10.1126/sciadv.adi7203